

The Role of Convectively Generated Gravity Waves on Convective Initiation: A Case Study

TAO SU AND GUOQING ZHAI

Department of Atmospheric Sciences, Zhejiang University, Hangzhou, China

(Manuscript received 23 May 2016, in final form 9 October 2016)

ABSTRACT

A case study of a convection initiation (CI) event involving a mesoscale gravity wave is presented. This severe convection event occurred in east China on 5 June 2009. High-frequency automatic weather station (AWS) data, visible satellite data, and Doppler radar data were combined to depict the features of the gravity wave and the development of several convection centers. The gravity wave was manifested by a surface pressure dip and surface wind shift propagating westward away from the early convection. The pressure dip propagated at a speed of $>30 \text{ m s}^{-1}$, which is comparable with that in previous observational studies of convectively generated gravity waves. A special focus is on the initiation of a deep convection cell in Anhui Province, which resulted in 25 deaths. Surface observations showed two precursors before CI, including a convergence line and wind shift at the eastern end of the convergence line. High-resolution numerical simulations with the Weather Research and Forecasting (WRF) Model were used to examine the structure of the gravity waves and forecast CI processes. The model reproduced the observed features of the gravity wave and the precursors before CI. Three-dimensional model results showed that CI occurred at the intersection between a convergence line and the gravity wave. The relationships between the wind shift and the pressure drop are consistent with polarization relation in ducted gravity waves. As the updraft of the gravity wave intersected with the convergence line, the low-level updraft strengthened and led to CI. The gravity wave, which had stronger updraft than downdraft, suggested a positive contribution to CI.

1. Introduction

Warm-season convective weather, together with low forecast skill, strongly affects many aspects of our economy and general livelihood (Fritsch and Carbone 2004). To improve the quantitative precipitation forecast skills, it is important to gain a better understanding of the processes of convective initiation (CI) and predict the timing and location of new convection (Browning et al. 2007; Weckwerth and Parsons 2006; Weckwerth et al. 2004). Boundary layer convergence lines (boundaries), detected by satellites as cloud lines and seen by radar as fine lines of enhanced reflectivity, are known to be potential loci of CI (Purdom 1976; Wilson and Schreiber 1986). The intersections of convergence lines (drylines, sea-breeze fronts, cold fronts, gust fronts, stationary convergence lines) with each other or with horizontal convective rolls create preferred locations for CI along the boundaries (Atkins et al. 1995; Koch and McCarthy 1982; Weiss and Bluestein 2002; Wilson and

Roberts 2006; Wilson et al. 1992; Xue and Martin 2006). The existence of preexisting clouds in advance of moving boundaries is also a key ingredient for CI (Hane et al. 2002; Kingsmill 1995; May 1999; Wilson and Mueller 1993). The along-line variability of updraft, temperature, and moisture influences the locations of CI along the boundaries (Crook 1996; Murphey et al. 2006; Wang and Xue 2012). Favorable vertical wind shear (Rotunno et al. 1988; Weisman and Rotunno 2004; Wilson et al. 1998) and thermodynamic distribution (Trier et al. 2015) are beneficial for convection initiation and sustenance, and it is essential that the moist boundary layer air parcels reach their lifting condensation level (LCL) and level of free convection (LFC) prior to leaving the boundary layer convergence zone (Ziegler and Rasmussen 1998).

Apart from the boundary layer processes, deep tropospheric gravity waves generated by convective heating of deep convection and their ability to initiate and organize convection are well documented (e.g., Bretherton and Smolarkiewicz 1989; Fovell 2002; Fovell et al. 2006; Lane and Reeder 2001; Lane and Zhang

Corresponding author e-mail: Guoqing Zhai, zhaigq@zju.edu.cn

2011; Mapes 1993; Nicholls et al. 1991). Convectively generated gravity waves can change the circulation near squall lines (Bryan and Parker 2010, hereafter BP10; Pandya and Durran 1996) and contribute to the maintenance of tropical mesoscale convective systems (MCSs) with weaker downdrafts (Lane and Moncrieff 2015). The partial gravity wave reflection between tropopause and ground underpins the formation of gravity wave modes whose vertical wavelengths are harmonics of the depth of troposphere. The numbers of antinodes in the vertical heating profile are typically used to label these modes. The deep fast wave mode, which has a vertical wavelength twice the depth of the troposphere, is referred to as the $n = 1$ mode. The $n = 1$ mode is generated by a heating profile that extends throughout the troposphere with its maximum at midlevels (Nicholls et al. 1991). The $n = 2$ mode and the $n = 3$ mode, which are characterized by ascent in the lower troposphere, have vertical wavelengths equal to the depth of the troposphere and two-thirds of the depth of the troposphere, respectively. The ascent of the $n = 2$ and $n = 3$ modes in the lower troposphere can reduce CIN, which produces favorable conditions for CI (Birch et al. 2013; Fovell et al. 2006; Lac et al. 2002; Lane and Zhang 2011; Mapes 1993). Waves of different modes travel in different speed. The speed of these waves is given by

$$c = \frac{NH}{n\pi}, \quad (1)$$

where N is the Brunt–Väisälä frequency, H is the vertical depth of the atmosphere, and n is the vertical mode of the heating profile (Nicholls et al. 1991).

In this paper, we present a case study of a severe convective event that involved both boundary layer CI processes and convectively generated gravity waves. This event, which occurred in east China on 5 June 2009, caused enormous economic loss and many casualties. We focused on a CI process that resulted from the combination of a gravity wave and a boundary layer convergence line. The gravity wave was generated by early convective systems and played a significant role in the CI process. The features of the gravity wave are simulated using a real-world model and the model results are compared with high-frequency observations.

There are few observational studies that have evaluated the modeling/theoretical features of convectively generated gravity waves. Adams-Selin and Johnson (2010) observed a surface low pressure feature rapidly propagating with little change in wind or temperature, which appeared to be the passage of an elevated, deep gravity wave. Numerical simulations proved that the surface wavelike feature was generated by $n = 1$ mode gravity waves (Adams-Selin and Johnson 2013, hereafter

ASJ13). BP10 observed similar surface features as well as evidence of ascent from soundings that could be attributable to $n = 1$ mode gravity waves. In the idealized modeling study of Nicholls et al. (1991), a pulse of heating generated an $n = 1$ wave, which consists of a downdraft-updraft couplet. The switch on of heating caused the downdraft of the wave that was accompanied by a low pressure perturbation at the surface and an increase in the flow toward the heating source at lower levels and away from the heating at upper levels. The switch off of heating caused the updraft of the wave, the return of the pressure, and wind fields to the initial state before the wave. Mapes (1993) suggested that the pre-storm environment is “permanently” modified by the downdraft of the wave, as the updraft of the wave does not appear until the convective system dissipates. The convective system was treated as long lasting heat source in their study, causing subsidence around the convective system and the absence of updraft; thus, the $n = 1$ waves were assumed to suppress new convection. However, it was noted by Lane and Zhang (2011) that the steady heat source that Mapes (1993) used to represent long-lived convective systems is not representative of short-lived or transient mesoscale convective cloud systems; thus, a periodic heat source is used in the simulations of Lane and Zhang (2011). An individual convective cloud could generate deep tropospheric gravity waves in the same way (Lane and Reeder 2001). Therefore, a transient heat source that can generate an $n = 1$ mode wave that consists of a downdraft–updraft couplet may be more representative of the convective activities. The surface wavelike features observed by Adams-Selin and Johnson (2010) and BP10 imply that $n = 1$ mode waves exist as downdraft–updraft couplets instead of only subsidence in the real world because of the transient heat of the convective activities.

Similar surface wavelike features are observed in the 5 June 2009 case. Although surface pressure disturbances caused by convectively generated gravity waves were observed in previous studies, surface wind disturbance features have not been emphasized. As far as we know, CI events related to the $n = 1$ mode gravity waves have not been documented to date. In this study, both the surface pressure and wind features are examined to manifest the passage of $n = 1$ gravity waves. CI episodes related to boundary layer processes and $n = 1$ gravity waves and their interactions are also presented. A nonhydrostatic mesoscale model is used to simulate these CI processes and examine the structure of the gravity waves.

The aim of this study is to determine if the surface pressure and wind features are generated by $n = 1$ mode gravity waves and, if so, to ascertain the effect of the waves on the CI process. Section 2 presents a review of

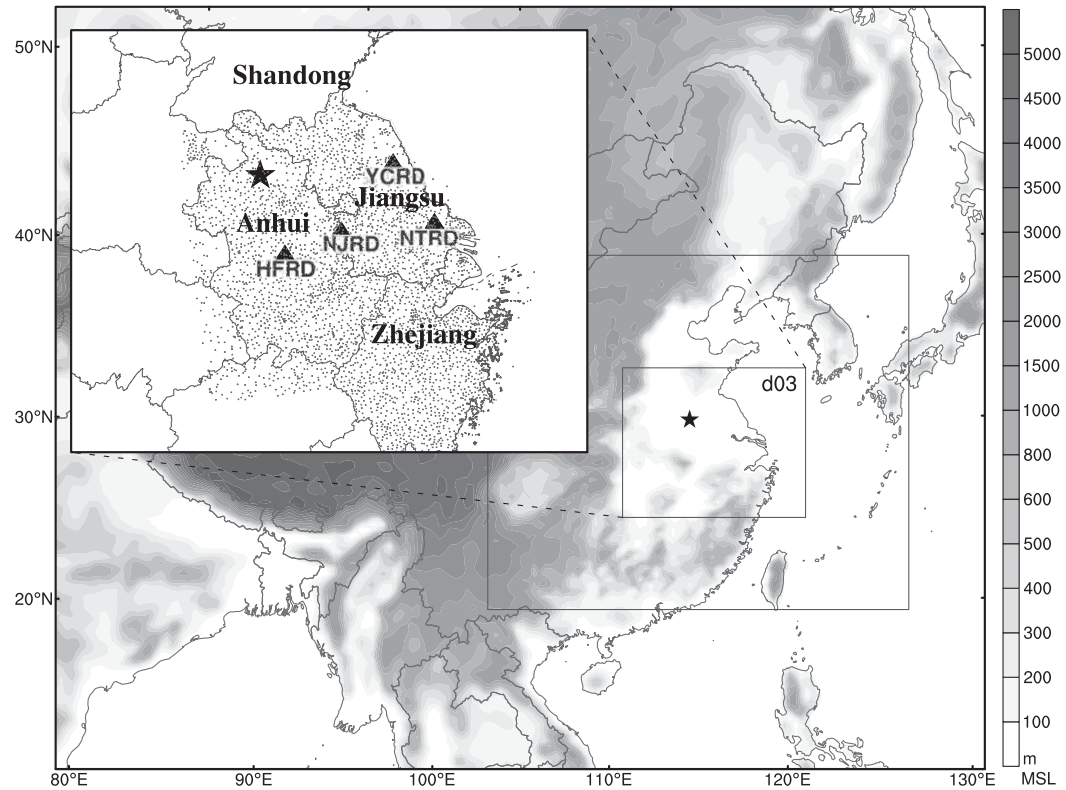


FIG. 1. The model domains with terrain elevation shaded. Rectangular boxes are the two model inner domains, with the innermost box enlarged. The filled triangles indicate the radar locations of Nanjing (NIRD), Yancheng (YCRD), Nantong (NTRD), and Hefei (HFRD). Boldface names are province names mentioned in the text. The stars indicate the location of the observed CI related to gravity wave (i.e., Cb). Small gray dots mark the locations of the automatic weather stations (AWSs) used in this study.

the case. Observational mesoscale analysis is given in section 3. The model experimental design and comparisons between simulation and observations are discussed in section 4. The structure of the simulated gravity waves and their role in CI are explored in section 5. A summary and discussion are given in section 6.

2. Overview of 5 June 2009

a. The MCS evolution

On 5 June 2009, severe convective weather occurred in the Shandong, Jiangsu, and Anhui Provinces of east China (refer to their locations in Fig. 1). This is one of the most severe weather events over the last few years in China, with 36 m s^{-1} strong winds, which resulted in 25 deaths in the Anhui Province. Figure 2 shows several CI episodes and the evolution of the convective cloud systems. The satellite pictures are drawn using the infrared IR1 data from the Japanese *Multifunctional Transport Satellite-1R (MTSAT-1R)* satellite. The primary convective cloud systems are labeled C1 to C5, and the two individually initiated cloud cells of C4 are labeled Ca

and Cb. At 0800 local standard time (LST = UTC + 8) 5 June 2009, a cold trough cloud system was moving southeastward following the steering wind in the mid-level troposphere. At 1000 LST, C1 was initiated in the coastal region of Shandong Province and moved toward the Jiangsu Province. C2 was initiated at 1200 LST and moved with the cold trough cloud system to the southeast. By 1400 LST, C1 and C2 had undergone remarkable development, whereas the Anhui Province was cloud free. During 1500 and 1700 LST, an isolated convective cloud labeled as Ca was initiated among the shallow clouds of 1500 LST in northern Anhui and a band of convective clouds labeled as C3 developed as C1 dissipated. After 1700 LST, another convective cloud labeled as Cb was initiated in northern Anhui and developed rapidly. It moved to the southeast with steering wind similar to Ca, forming a cloud cluster labeled as C4. By 1900 LST, the southeast-moving C4 and the west-moving C3 merged into a large MCS labeled as C5.

Among these cloud systems, Cb was initiated in the cloud-free area near C1 and C3, which was likely influenced by secondary initiation mechanisms. On the other

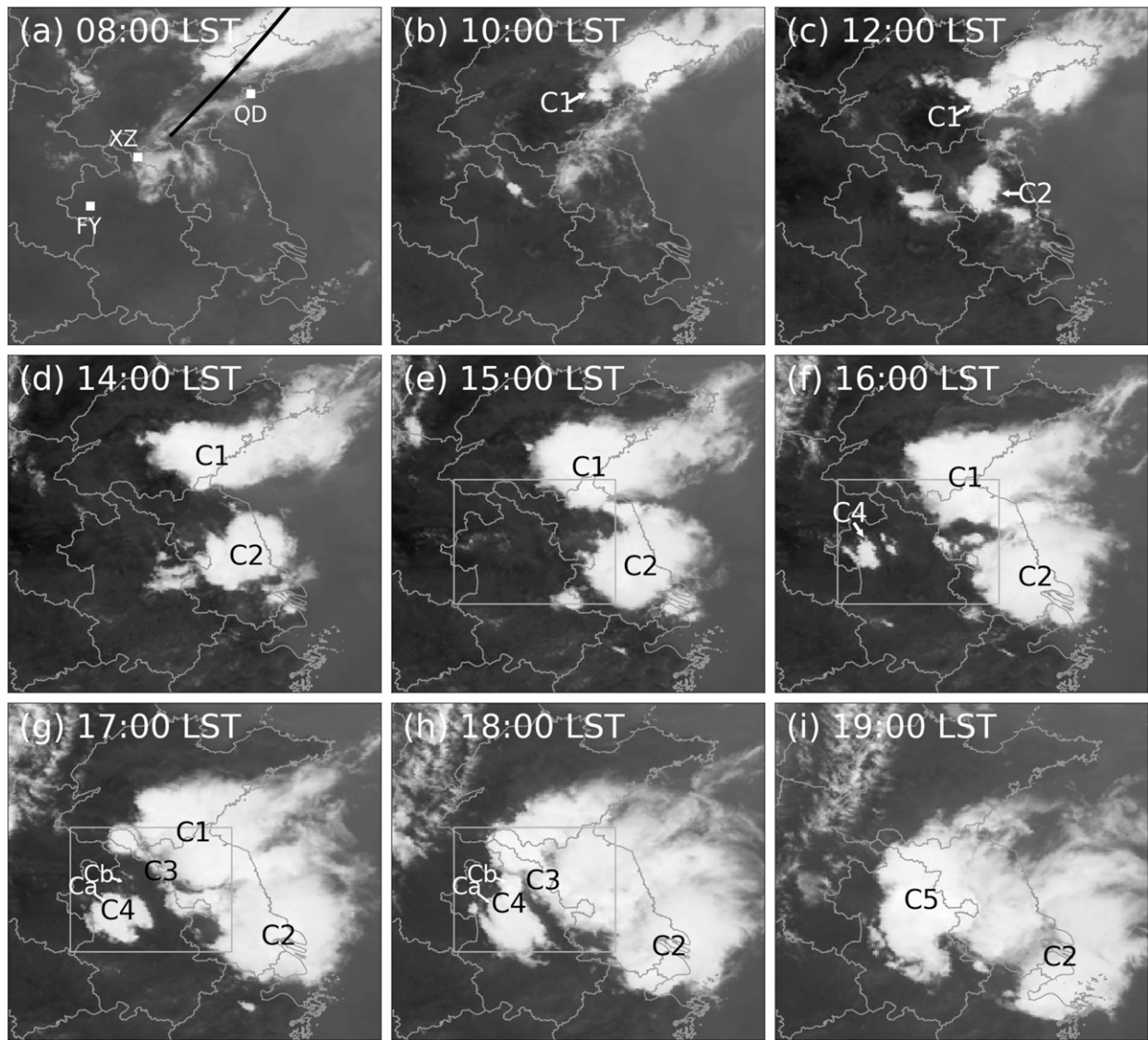


FIG. 2. Infrared satellite pictures from Japanese *MTSAT-1R* satellite from 0800 to 1900 LST 5 Jun 2009. Also shown are province boundaries (gray lines). Province names are labeled in Fig. 1. Convective clouds are numbered from C1 to C5. Locations of station Qingdao (QD), Xuzhou (XZ), and Fuyang (FY) are marked with filled squares in (a). Gray square boxes in (e)–(h) show the domains of Fig. 5.

hand, Cb developed into a deep convection with a destructive gust front that resulted in the loss of life. Therefore, the initiation of the cloud feature Cb, whose location is marked by the filled star in Fig. 1 and other figures, is specifically focused on in this study.

b. Synoptic situation

Figure 3 shows the major synoptic features when the severe weather event happened. The synoptic situation was characterized by a deep and cold vortex over northeast China, known as the northeast China cold vortex (NCCV). Cold vortices are slow-moving cold-core cyclonic centers in the mid- to upper troposphere.

Cold-vortex circulation is a typical pattern for the formation of squall lines in east China (Meng et al. 2013). By 1400 LST 5 June, the cold-vortex circulation had existed for more than 3 days over northeast China. Seen from the 500- and 850-hPa levels, the cold-vortex center was located at about 45°N, 125°E. In the cold-vortex pattern, the primary CI locations are related to the propagating path of the trough (Meng et al. 2013). At the 500-hPa level, a trough was propagating to the southeast, following an earlier trough in south China. At 0800 LST, the bottom of the trough was in Shandong Province (thick gray line in Fig. 3a) and a cloud system was moving with the trough. The C1 and C2 cloud

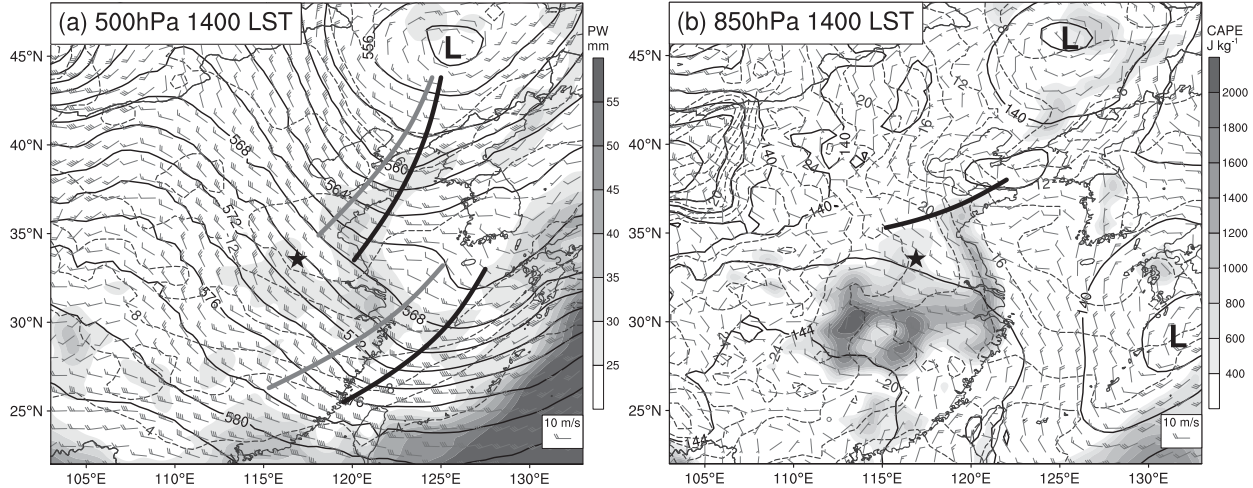


FIG. 3. Geopotential height (solid black contours, 10 m), temperature (dashed gray contours, °C), and wind barbs (one full barb = 5 m s^{-1}) at 1400 LST 5 Jun 2009 at (a) 500 and (b) 850 hPa. Also shown are (a) precipitable water (gray shaded, mm) and (b) CAPE (gray shaded, J kg^{-1}). Gray bold lines indicate the locations of trough lines at 0800 LST, black bold lines indicate the locations of trough lines at 1400 LST. Filled stars indicate the same CI location as Fig. 1.

systems were initiated before this trough between 0800 and 1400 LST (section 2a). By 1400 LST, before Ca and Cb were initiated, the 500-hPa trough line had moved to the middle of Jiangsu Province, leaving all the northern Anhui behind the 500-hPa trough line (thick black line in Fig. 3a). At the 850-hPa level, the northern Anhui was in the northwest flow with warm advection in front of the trough (Fig. 3b). The overlaying of the cold air at 500 hPa on the warm air at lower level provided favorable conditions for the initiation of C4. In summary, C4 was initiated behind the 500-hPa trough and in front of

the 850-hPa trough, which is also a typical environment flow pattern of squall lines in north China (Ding 1992), whereas C1 and C2 was initiated before the 500-hPa trough and the large temperature lapse rate in the cold-vortex environment provided generally unstable environments for CI.

Figure 4 shows the soundings released at 0800 LST for three stations in Fig. 2a: Qingdao (QD), Xuzhou (XZ), and Fuyang (FY). The Qingdao sounding is representative of the environment when C1 was initiated. Even though C2 was initiated about 100 km southeast of

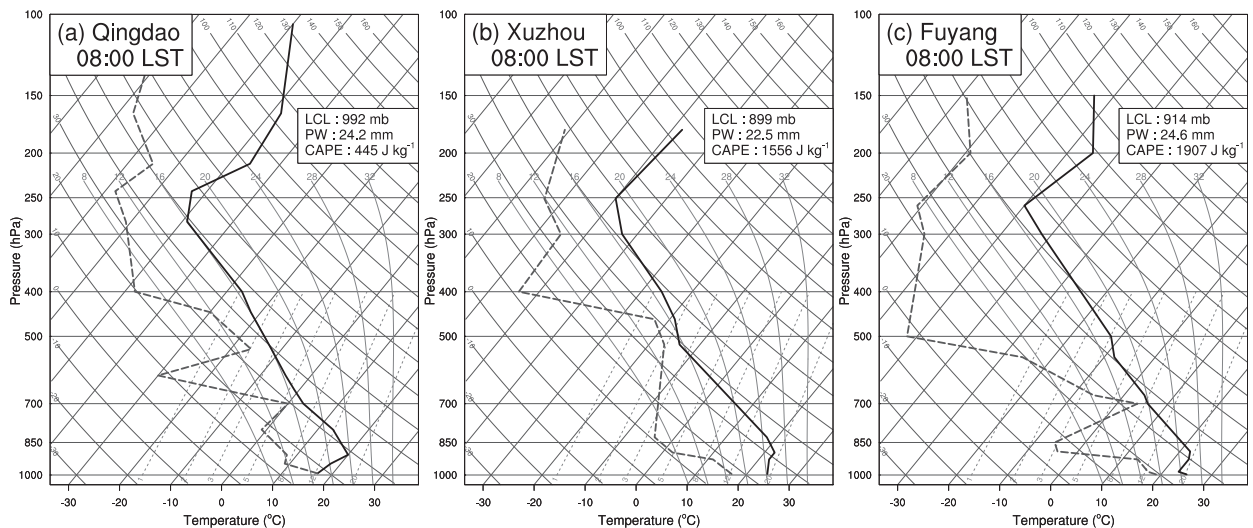


FIG. 4. Skew T-logP plots of soundings of temperature (solid black lines) and dewpoint temperature (dashed gray lines) over (a) Qingdao, (b) Xuzhou, and (c) Fuyang sounding stations at 0800 LST 5 Jun 2009. The station locations are marked on the satellite image at 0800 LST in Fig. 2a.

Xuzhou 4 h later, C2 was initiated among the southeast-moving clouds that passed over Xuzhou at 0800 LST; thus, the Xuzhou sounding is representative of the environment where C2 was initiated. Both the Qingdao and Xuzhou soundings show a moist layer at 500 hPa ([Figs. 4a and 4b](#)). This feature is consistent with the configuration highlighted in previous studies (e.g., [ASJ13; BP10](#)) as favorable to the generation of $n = 1$ gravity waves. The nearly saturated moist layer at 500 hPa suggests that the trough cloud system was at approximately 500-hPa height. The Fuyang sounding ([Fig. 4c](#)) represents the post-trough environment with a dry layer at 500 hPa. The precipitable water was below 30 mm in all three stations. Although water vapor was not abundant in the atmosphere, the moist air transported by the sea breeze sustained C1 and C2 longer along the coastal region ([Figs. 2d–g](#)).

3. Mesoscale analysis

a. CI observations

Fengyun 2C (FY2C) 1-km visible satellite images obtained every 30 min show more details of the initiation of the convective clouds ([Fig. 5](#)). A gust front generated by C1 appeared as an arc-shaped cloud line, as [Purdom \(1976\)](#) described (white dashed line in [Fig. 5a](#)), which was supposed to trigger new convection. The arc-shaped cloud line was moving westward out from the decaying thunderstorm region to Anhui Province ([Figs. 5b,c](#)). At 1600 LST, a slow-moving shallow cloud line formed along the border of Jiangsu and Anhui in front of the gust front. Two convective cloud cells were embedded in the cloud line, one of which was near Xuyi and the other was to the northeast of Xuzhou. The gust front did not trigger deep convection until it intersected the shallow cloud line ([Fig. 5d](#)). The shallow cloud line was probably caused by a low-level convergence line; however, the convergence line was not obvious in surface observations (not shown). The subsequent convective cells were inhomogeneous along the gust front ([Fig. 5e](#)). One center (labeled C3a) formed near Xuzhou where the gust front came across the existing cloud cell, and the other center (labeled C3b) formed near the “triple point” where the gust front and the cloud line intersected ([Fig. 5c](#)). C3a, C3b, and the new convective clouds between them are labeled C3 in the rest of the discussion.

Observations of three weather stations near Cb ([Fig. 6](#)) and radar observations ([Fig. 7](#)) are presented to support the satellite observations analysis. As C3 was initiated along the gust front, Cb was initiated among shallow clouds near Suzhou almost at the same time and about 100 km in front of the gust front ([Fig. 5d](#)). By the time the gust front approached Suzhou at 1730 LST, Cb

had developed into a deep convection almost as strong as C3 ([Fig. 5e](#)). By 1800 LST, the radar reflectivity of Cb had exceeded 60 dBZ, while the gust front had just reached the edge of Cb ([Fig. 7a](#)). The position of the gust front can be estimated by the moving weak reflectivity belt outlined by the black lines ([Fig. 7a](#)). The surface temperature and wind speed also showed a sharp gradient indicating the gust front northeast to Cb at 1800 LST. The gust front arrived at station A, approximately the center of the developed Cb, at 1830 LST, by which time the precipitation produced by Cb had lasted for half an hour ([Fig. 6a](#)). Therefore, the gust front could not be the direct trigger mechanism of Cb. On the other hand, Ca did not develop into deep convection that could generate the gust front that could trigger Cb either. The observations at stations B and C ([Figs. 6b and 6c](#)) show that when the Ca clouds moved above the stations between 1530 and 1700 LST ([Figs. 5a–d](#)), there was only a slight decrease in temperature (still above 30°C) with no precipitation or gust front. It was the gust front generated by Cb that eventually brought rainfall to stations B and C ([Fig. 7b](#)).

The wind speed of the gust front related to C3 was 20 m s⁻¹ at its maximum ([Fig. 6a](#)), whereas the wind speeds of the gust front in [Figs. 6b and 6c](#) were over 30 m s⁻¹ at their maximum, which proved that the gust front could only be generated by Cb. The strong wind of this gust front caused many deaths on the night of 5 June 2009. Thus, it is crucial to find out how Cb was initiated in this sense.

b. Surface features near the CI cloud system

[Figure 8](#) shows surface observations from six weather stations (white dots in [Fig. 5](#)) between C1 and C3. The observations suggest that the gust front denoted by the cloud line in [Fig. 5](#) passed all these stations. The gust front passed stations S1 and S2 at approximately 1500 and 1510 LST, respectively (gray vertical lines in [Figs. 8c and 8f](#)), before being captured by satellites. It arrived at station S3 at 1540 LST ([Fig. 8b](#)), which is consistent with the fact that the cloud line was approaching station S3 at 1530 LST (white dashed line in [Fig. 5a](#)). The cloud line formed by the gust front was beneath the anvil of C1 at 1530 LST ([Fig. 5a](#)); thus, only part of the cloud line was clear and outlined by the white dashed line. The gust front passed stations S4 and S5 at the same time ([Figs. 8a and 8e](#)), both at 1600 LST. On the satellite images, the cloud line had moved to station S5 by 1600 LST also ([Fig. 5b](#)). It is difficult to tell whether the cloud near station S4 was formed by the gust front only based on the satellite images, because it was situated at the same location before the anvil and showed little movement in contrast to the cloud line outlined by the white dashed

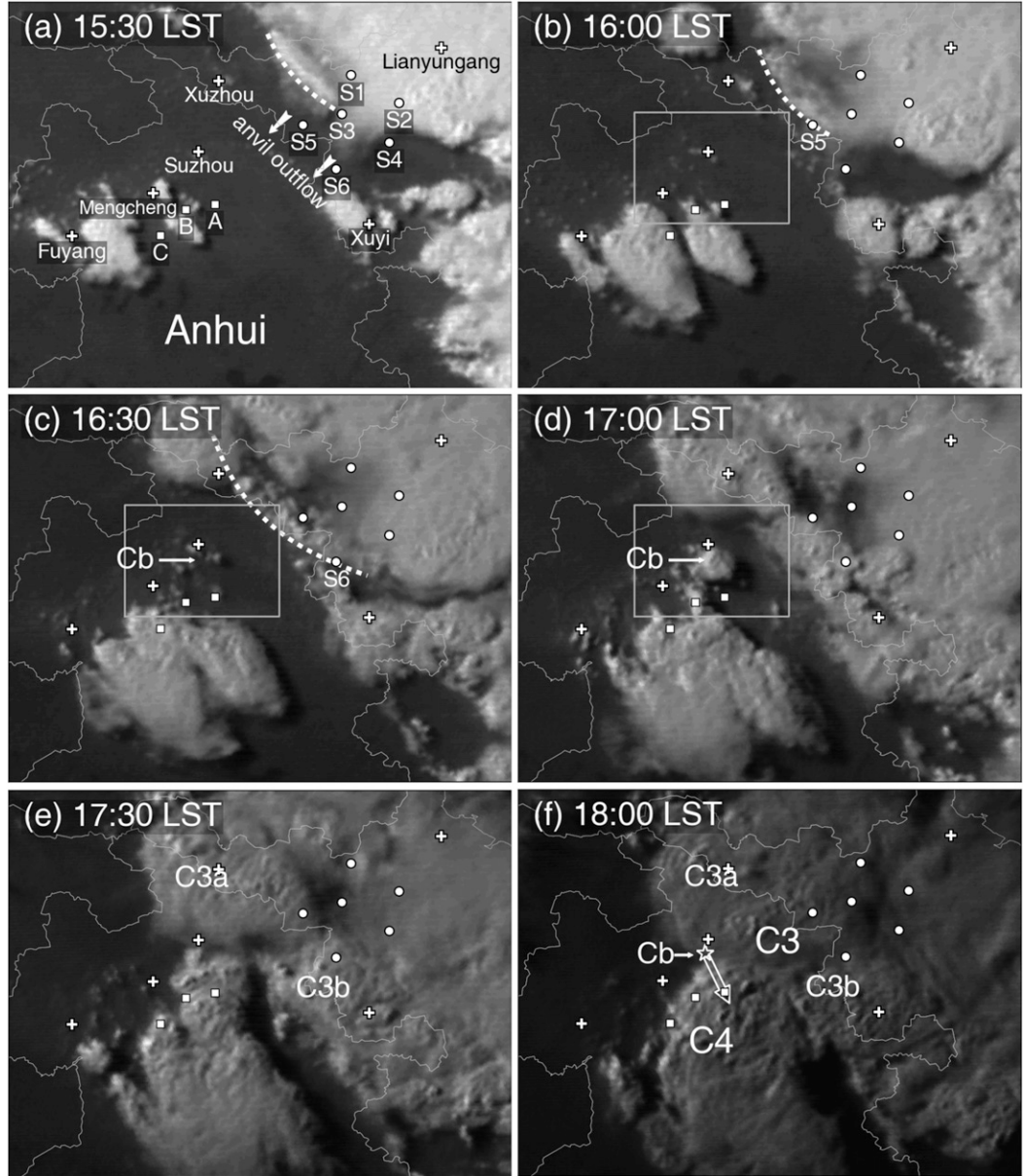


FIG. 5. FY high-resolution visible satellite images at (a) 1530, (b) 1600, (c) 1630, (d) 1700, (e) 1730, and (f) 1800 LST 5 Jun 2009. Convective clouds C3 and C4 are labeled. Relevant cities and stations are labeled in (a). White squares represent stations for reference in Fig. 6 while white dots represent stations for reference in Fig. 8. Gray square boxes show the domains of observed CI in Fig. 11. The hollow star and hollow arrow in (f) indicate the initiation location and moving direction of Cb.

lines. However, combined with surface observations, the gust front extended to station S4 in an arc shape. The gust front passed station S6 at 1640 LST (Fig. 8d), corresponding to the cloud line that had become more convective at 1630 LST (Fig. 5c). Also evident is the second gust front manifested by the second pressure jump accompanied by the slight shift in the wind direction and unaccompanied by another temperature decrease (e.g., Figs. 8e,f). This gust front is believed to

be generated by the convective cells to the south of Lianyungang (Fig. 5b), whereas the first gust front was generated by the convective cloud in C1 near Lianyungang (Fig. 2d, also shown in Fig. 9). The second gust front was not the primary trigger system during this case; however, it proved that a strong precipitating convective cloud occurred as C1 decayed, which was capable of generating gravity waves. There is also evidence that the gust front did not trigger deep convection and cause

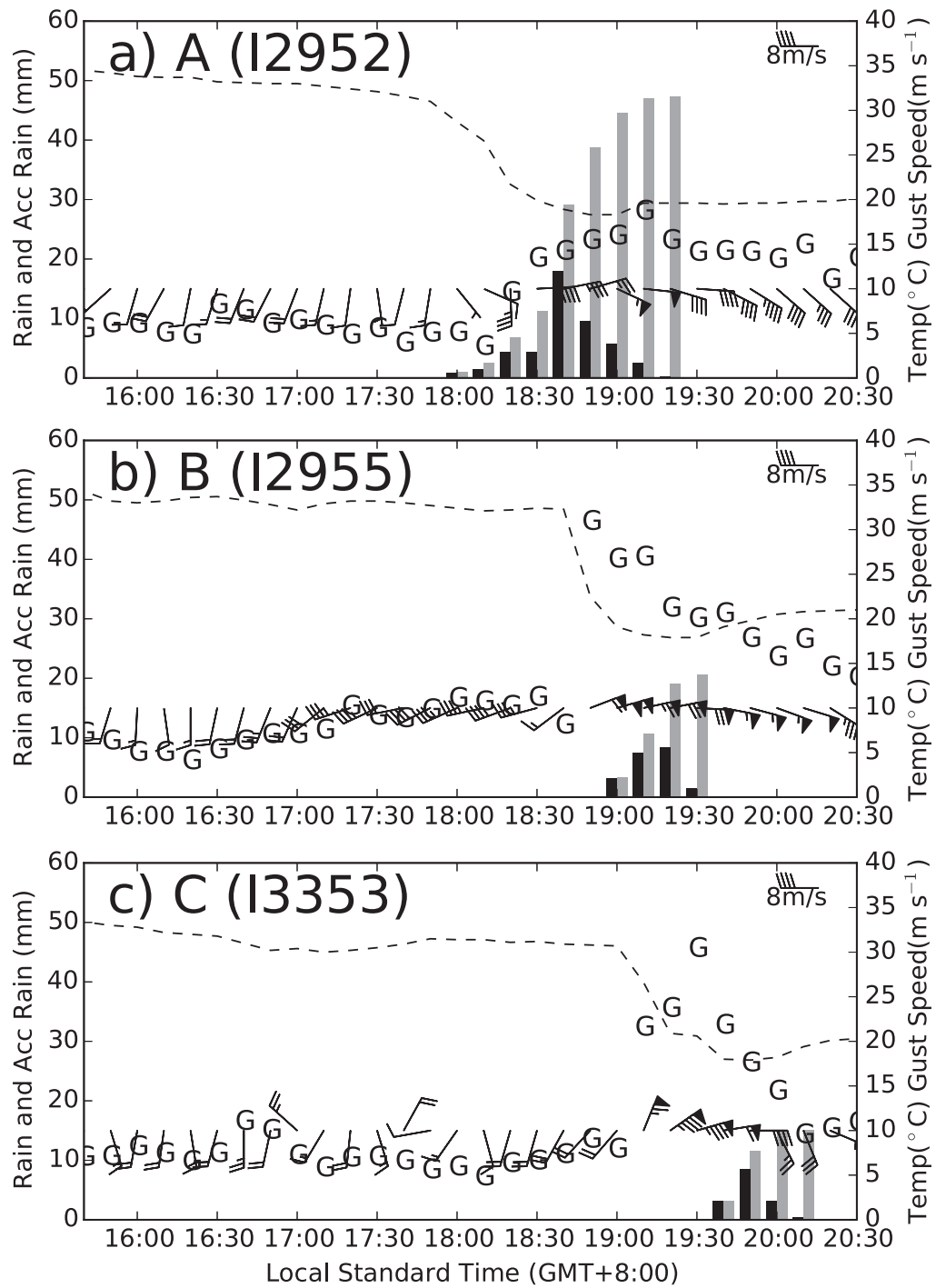


FIG. 6. Time series of temperature (dashed lines, $^{\circ}\text{C}$), wind (full and half barbs represent 2 and 1 m s^{-1} , respectively), 10-min precipitation (black bars, mm), accumulated precipitation (gray bars, mm), and maximum wind speed in 10 min (marked by “G,” m s^{-1}) at stations (a) I2952 (labeled as A in Fig. 5), (b) I2955 (B), and (c) I3353 (C). Station locations are shown in Fig. 5.

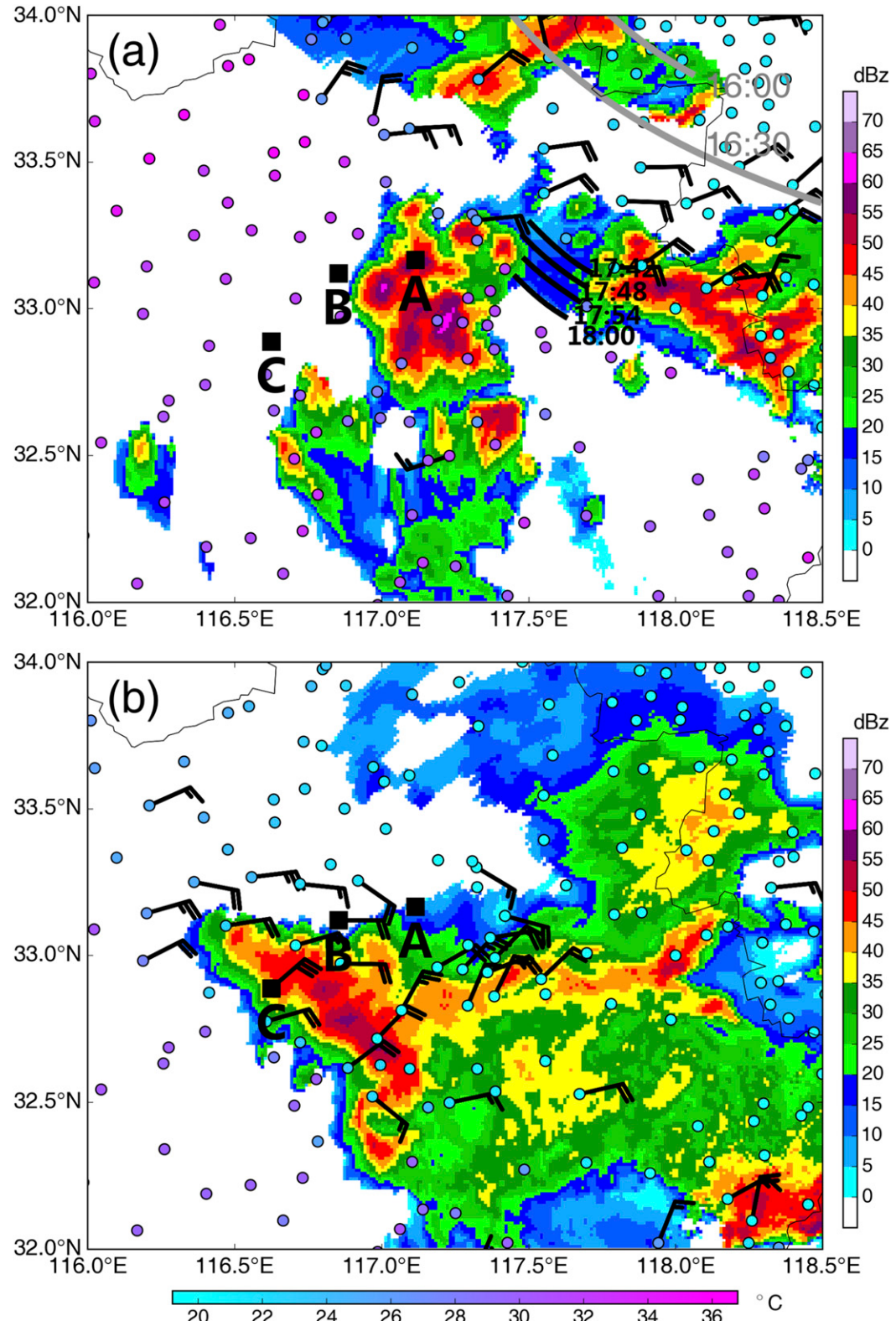


FIG. 7. Radar reflectivity of 0.5° elevation at the Nanjing radar station (location shown in Fig. 10) and temperature (colorful dots, °C) at the AWSs at (a) 1800 and (b) 1930 LST. Also shown are wind barbs with maximum wind speed in 10 min exceeding 15 m s^{-1} (full and half barbs represent 10 and 5 m s^{-1} , respectively). The gray lines in (a) are the white dashed lines in Fig. 5. The short black lines in (a) denote the positions of the gust front before 1800 LST.

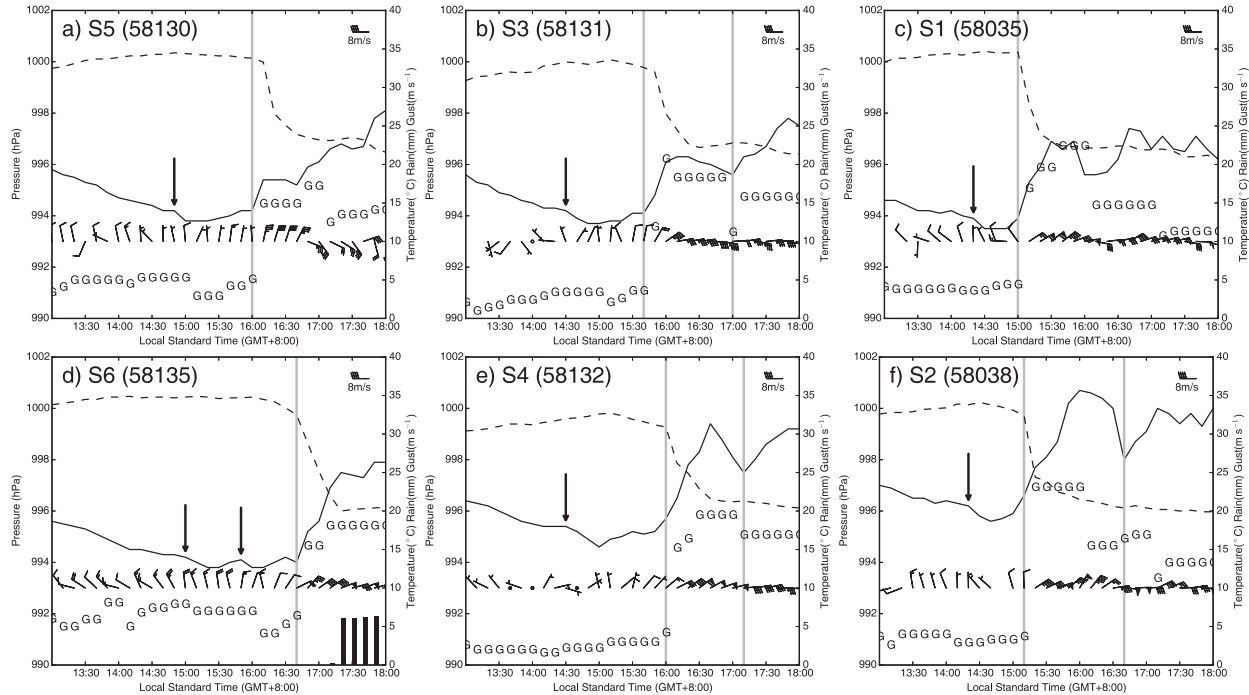


FIG. 8. Time series of pressure (solid lines, hPa), temperature (dashed lines, °C), wind (full and half barbs represent 2 and 1 m s⁻¹, respectively), accumulated precipitation (black bars, mm), and maximum wind speed in 10 min (marked by “G,” m s⁻¹) at stations (a) 58130 (labeled as S5 in Fig. 5), (b) 58131 (S3), (c) 58035 (S1), (d) 58135 (S6), (e) 58132 (S4), and (f) 58038 (S2). Station locations are shown in Fig. 5. The vertical gray lines denote the passage time of gust fronts. The downward arrows denote the beginning of the pressure dip at each station.

precipitation until C3 developed. Among the six stations, only station S6 near C3 recorded precipitation (Fig. 8d).

Before the arrival of the gust front, a dip in pressure embedded within the synoptic-scale pressure fall is

noted at these stations. The solid arrows in Fig. 8 denote the beginning of the dip at each station. The dip is indicative of a gravity wave and is most evident in stations S6 and S4 (Figs. 8e and 8d); the pressure rises after the

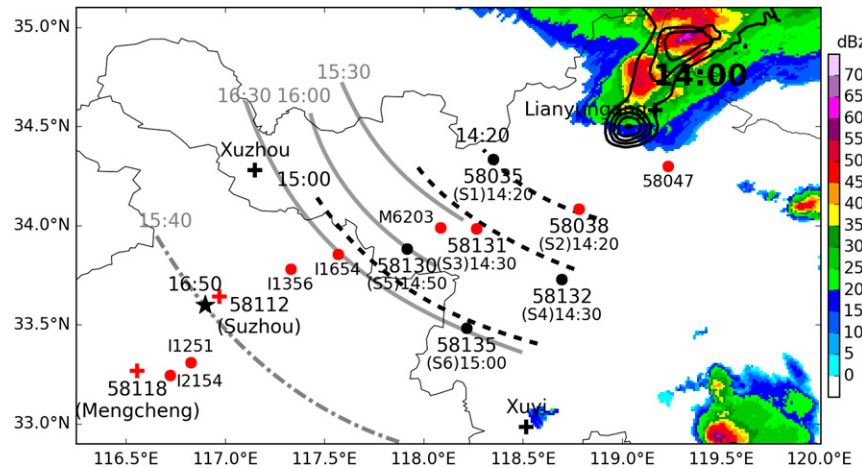


FIG. 9. Isochrones (black dashed lines, every 20 min) for the beginning of the pressure dip denoted by solid arrows in Fig. 8. The time is presented under the station number at each station. Gray dot-dashed line indicates the extrapolated time for the dip. Gray lines are the white dashed lines in Fig. 5, denoting the positions of the gust front at 1530, 1600, and 1630 LST. Also shown are radar composite reflectivity (shaded, dBZ), and 1-h precipitation between 1400 and 1500 LST (black contours, mm). Red markers denote the stations selected for the Hovmöller diagram in Fig. 12.

dip. However, considering the synoptic-scale variation, a negative pressure perturbation exists in other stations as well. Based on the time the dip arrived at each station, it is apparent that the dip was propagating in the same direction with the gust front. When the dip passed stations S1 and S2, the gust front followed closely to the dip ([Figs. 8c and 8f](#)). When the dip arrived at stations S5 and S6, the gust front fell behind the dip to a larger distance, suggesting that the dip propagated faster than the gust front ([Figs. 8e and 8d](#)). The propagating dip is similar to the one observed by ASJ13 that also propagated fast in front of a gust front, but with weaker amplitude. The weaker signature is attributed to the data sampled at 10-min intervals (5 min in ASJ13) which could lose some of the wave signature, as illustrated by [Jacques et al. \(2015\)](#), or it is related to the strength of gravity wave that produced the surface pressure dip.

The isochrones of the pressure dip are shown in [Fig. 9](#) (black dashed lines). The surface distance between stations S2 and S6 is 84.8 km and it takes 40 min for the pressure dip to travel this far, from which a speed of 35.3 m s^{-1} can be calculated. Considering the gravity wave front is not normal to the direction of S2 to S6, the gravity wave traveled less than 84.8 km; thus, the wave speed is less than 35.3 m s^{-1} (e.g., 33 m s^{-1} for 80 km). Based on [\(1\)](#), the typical $n = 1$ wave speed is approximately 30 m s^{-1} . Therefore, the estimated wave speed is indicative of an $n = 1$ gravity wave. Taking the more accurate isochrones of the gust front (gray solid lines) as reference, the gravity wave travels almost twice as fast as the gust front. By 1500 LST, when the gust front arrived at stations S1 and S2, the front of the gravity wave had arrived at station S6. The wave arrived at the CI location of Cb cloud at 1540 LST by extrapolation, and Cb was initiated after about 1 h. Although features of an $n = 1$ gravity wave are observed, the determination of the features of the gravity wave and the wave's role in Cb's initiation requires a numerical model.

4. Model experiments and results

a. Model configuration and verification

The WRF Model, version 3.4.1 ([Skamarock et al. 2008](#)), was used in the numerical simulation of the gravity wave and CI processes. The two-way nested model domains are shown in [Fig. 1](#). The domains have 36-, 12-, and 4-km grid spacing, respectively, with 42 vertical levels and a model top at the 50-hPa level. The inner domain covers Jiangsu, Anhui, and part of the Shandong Province, where the severe convective weather mainly occurred. The simulation was initialized at 2000 LST 4 June 2009 by Japan Meteorological Agency's (JMA) Regional Spectral Model 20-km reanalysis data

(RSM-20km; [NPD/JMA 1997](#)), which also provided the lateral boundary conditions updated every 6 h. The WRF single-moment 6-class microphysics scheme (WSM6; [Hong and Lim 2006](#)) was used. This scheme accounts for the resolvable-scale convection with explicit treatment of cloud water, rainwater, snow, cloud ice, and graupel. The Kain–Fritsch (KF) cumulus parameterization ([Kain 2004](#)) was applied on the outer 36- and 12-km domains only. Other physical parameterization schemes include the Yonsei University (YSU) planetary boundary layer model ([Hong et al. 2006](#)), the Noah land surface model (LSM) with four soil levels ([Chen and Dudhia 2001](#)), the Rapid Radiative Transfer Model for General Circulation Models (RRTMG) longwave radiation scheme ([Iacono et al. 2008](#)), and the Dudhia shortwave radiation scheme ([Dudhia 1989](#)).

Data were assimilated by the 3DVAR approach of the WRF Data Assimilation System (WRFDA) with 1-hourly rapid cycles for the assimilation window from 1200 to 1500 LST. A free forecast was then run from 1500 to 2000 LST 5 June 2009. The data assimilated are surface data from stations mainly in Anhui, Jiangsu, and Zhejiang Provinces (small dots in [Fig. 1](#)) and radar reflectivity data from four radar stations (filled triangles in [Fig. 1](#)).

[Figure 10](#) shows the evolution of the simulated convections compared with observations. During the assimilating time window, the C1 and C2 cloud systems were well reproduced by the model simulations ([Figs. 10a and 10b](#)) before C3 and C4 occurred, with C2 simulated stronger than observed and noticeable location errors of C1 at 1410 LST. By comparing these to simulations without assimilation (not shown), we believe the assimilation of the radar reflectivity data improved the moisture distribution, leading to the simulated convection developing toward the locations of observed convections. During the forecast period, the initiation of the C3 cloud system, which was caused by the gust front of the dissipating C1, was well predicted ([Figs. 10c and 10d](#)). The southern end of C3 was predicted west of the observations, probably owing to a stronger gust front generated by the more intense C2. In the model, a new cell initiated prior to the arrival of the gust front and moved southeastward. These two characteristics correspond to the observed Cb cloud; therefore, this cell is designated as Cb. The predicted Cb has a time delay of 30 min and occurs about 60 km southeast of the observed one. The 4-km horizontal grid spacing is nominally sufficient to explicitly represent the convection without the need for parameterization ([Weisman et al. 1997](#)). However, such grid resolution is insufficient to resolve the details of convection ([Bryan et al. 2003](#)). In this study, we are interested in the initiation mechanism of Cb rather than the structure and evolution of the

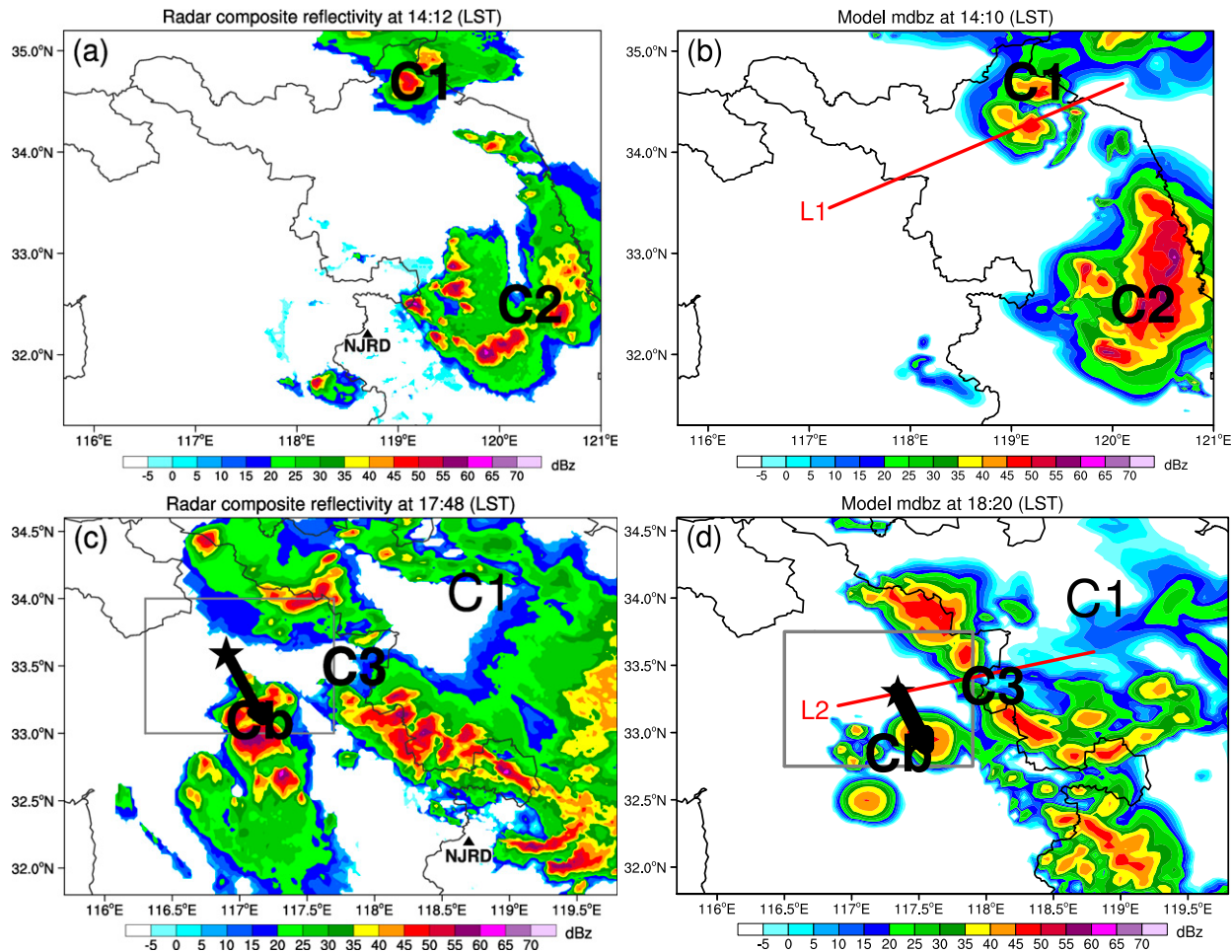


FIG. 10. Observed radar composite reflectivity of Nanjing radar station (denoted by black triangle) at (a) 1412 and (c) 1748 LST and WRF forecast radar composite reflectivity at (b) 1410 and (d) 1820 LST. Filled stars denote the CI locations of Cb in observation and simulation. Gray square boxes show the enlarged domains in Fig. 11.

convection, and the 4-km grid is able to resolve mesoscale systems that initiated Cb.

Figure 11 shows observations (left) and model results (right) for the surface wind fields when Cb was initiated. The surface wind observations show a steady horizontal convergence line (black dashed line in Fig. 11a) that formed by northwesterly flow and southwesterly flow at 1530 LST. This convergence line had existed since 1400 LST (not shown) and still existed when Cb occurred at 1710 LST (Fig. 11e). However, there was a sudden wind shift at the eastern end of the convergence line at 1650 LST, as indicated by the black arrows in Fig. 11c. By this time, the gust front had not reached this region since the temperature had not dropped much (Figs. 7a and 11d). The veering of wind was obvious and simultaneous at several stations along the gray dashed line in Fig. 11c at 1650 LST. There was an increase to the northeast wind component, approximately normal to the gray dashed line. As a result, the northwesterly wind turned nearly

north and the southwesterly wind turned southeasterly. By 1710 LST (Fig. 11e), the wind component increased further, and Cb was initiated near the eastern end of the convergence line. Therefore, the convergence line and the wind shift were two precursors of the CI, and the model reproduced them both (Figs. 11d and 11f). Note that the simulated convergence line was southeast of the observed one, leading to the spatial shift of Cb's initiation. Besides, the simulated wind shift occurred half an hour later than observed, corresponding to the delay of Cb's initiation. Despite the shift in the model results, the timing and location of Cb's initiation relative to the precursors were well predicted. This suggests that the model simulation of the mechanisms of Cb's initiation is realistic and further analysis of the model output can be performed.

b. Surface wind features of Cb's initiation

Slight wind veering is noticeable at stations near the cloud feature C1 accompanied by the pressure dip

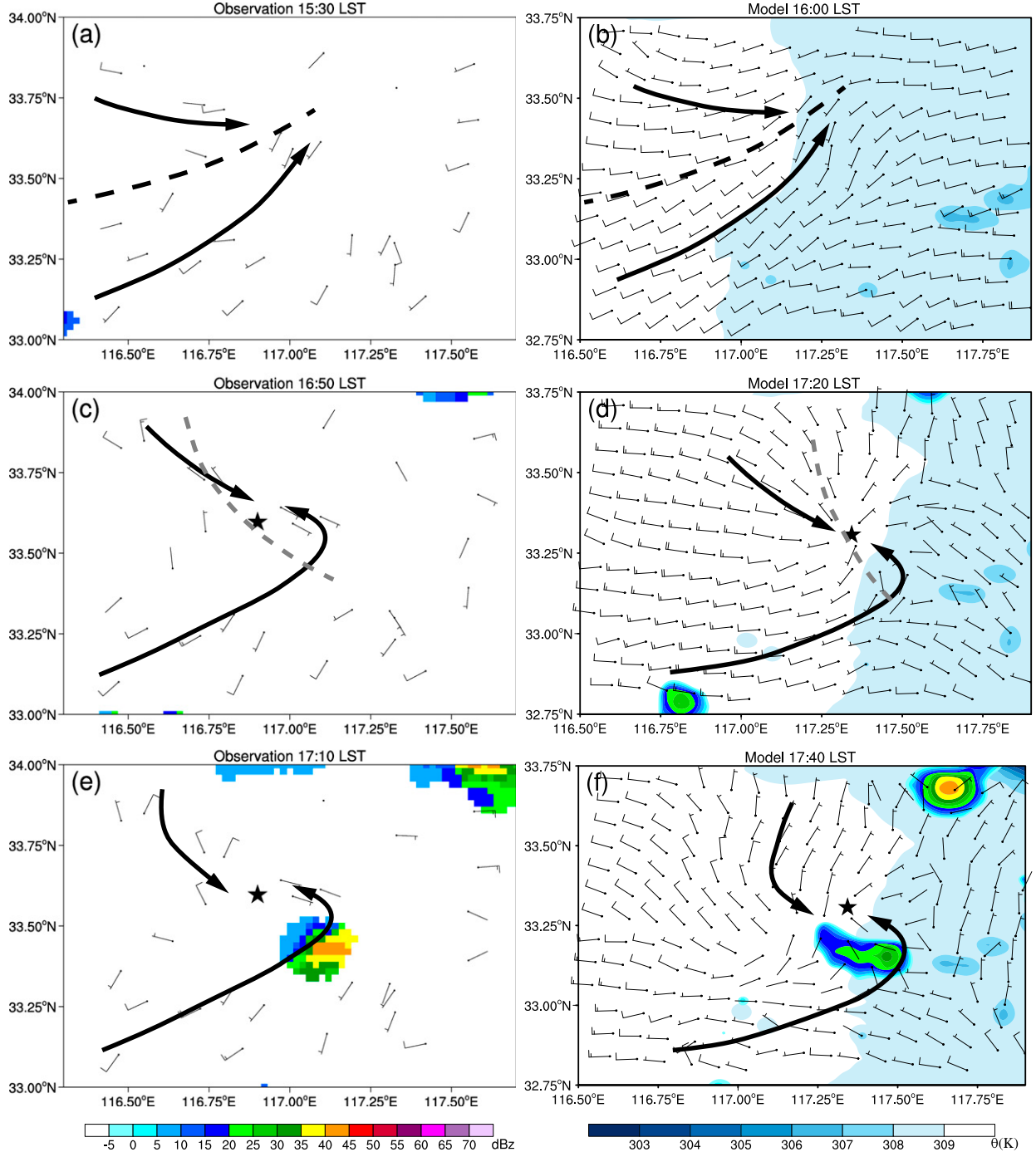


FIG. 11. Observed composite reflectivity fields (shaded, dBZ) and surface wind barbs (full and half barbs represent 4 and 2 m s⁻¹, respectively) at (a) 1530, (c) 1650, and (e) 1710 LST 5 Jun 2009, and WRF forecast composite radar reflectivity fields (shaded, dBZ) and streamlines at 10 m AGL at (b) 1600, (d) 1720, and (f) 1740 LST 5 Jun 2009. Filled stars mark the CI locations of Cb cloud in observation and model prediction.

described in section 3b (e.g., 1440 LST in Fig. 8b). The wind veering propagated westward to Anhui Province where Cb was initiated and forced the wind toward the propagating direction. To illustrate how the wind veering

propagated in the observations and in simulation, Hovmöller diagrams with approximately east–west-oriented x axis are presented for comparison (Fig. 12). The gust front generated by C1 was propagating to the west (black

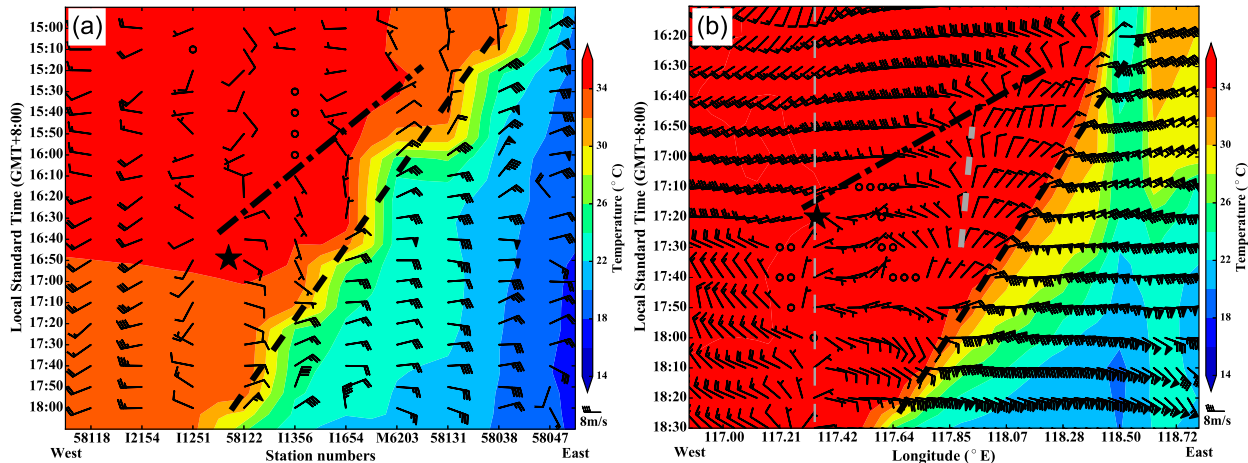


FIG. 12. Hovmöller diagrams of temperature (shaded, $^{\circ}\text{C}$) and wind (full and half barbs represent 2 and 1 m s^{-1} , respectively) of (a) observation and (b) WRF simulation. The locations of the x axis in (a) are shown by the red markers in Fig. 9, and the locations of the x axis are along the red line named L2 in Fig. 10d. The dashed black lines indicate the moving of gust fronts, and the dot-dashed lines denote the temporal evolution of wind shift. The thick dashed gray line denotes the location of a stationary convergence line. The thin dashed gray line denotes the primary CI location.

dashed lines), leading to substantial increase in wind speed and substantial decrease in temperature. The wind veering denoted by the black dot-dashed lines occurred before the wind shift to strong easterlies associated with the gust front. The smaller slope of the dot-dashed line suggests that the wind veering propagated at a larger speed than the gust front. Wind veering toward the direction of the gust front occurring prior to the gust front could be caused by a bore (Koch and Clark 1999; Locatelli et al. 1998). A bore is a gravity wave disturbance generated when a density current intrudes into a stable stratified layer near the ground. However, there was no stable layer by the afternoon, which suggests the absence of a bore. Therefore, the wind veering can only be caused by the fast-propagating $n = 1$ wave.

There was a quasi-stationary convergence line before the gust front (gray dashed line in Fig. 12b), which was not resolved by surface observations. The location of this convergence line corresponded to the location of C3's initiation, suggesting that C3 was initiated by the interaction of the convergence line and the gust front. In the observations, although this convergence line was not found in the surface analysis owing to limited data resolution, there was a quasi-stationary shallow cloud line that indicated the convergence line. In the observations and the simulation, Cb was initiated within 10 min after the wind shift arrived (black stars in Fig. 12), which suggests this wind shift was an important precursor to Cb's initiation.

High-resolution model output data were used to further investigate the mechanism of Cb's initiation. Figure 13 shows the evolution of the surface wind fields

and divergence fields before Cb was initiated. The convergence line indicated by the black dashed line in Fig. 11b is characterized by an approximately west–east-oriented elongated convergence zone (Fig. 13a). A divergence–convergence couplet propagated westward and intersected with the convergence line. By 1710 LST, the divergence zone of the couplet intersected with the convergence line near point A and the convergence zone of the couplet intersected with the convergence line near point B (Fig. 13b). As a result, the convergence value near point A became much smaller, whereas the convergence value near point B increased substantially. The wind veering followed the passage of the convergence zone of the couplet. The wind shift near point B was most apparent, changing from west to east in a short time (Figs. 13c and 13d; see also the vertical dashed gray line in Fig. 12b). Cb was initiated near point B where the convergence was at its maximum along the convergence line at 1720 LST (based on the cloud water mixed ratio in Fig. 14c). Overall, the wind veering was related to the divergence–convergence couplet, and the CI location corresponded to the area where the strongest convergence occurred owing to the intersection of the couplet with the convergence line.

The fast-moving divergence–convergence couplet in the model also suggested a gravity wave. The divergence zone corresponded to negative vertical velocity at 6-km height (dashed contour lines in Fig. 13) and the convergence zone corresponded to positive vertical velocity at 6-km height (solid contour lines in Fig. 13). The vertical structure of this gravity wave is shown in detail in section 5.

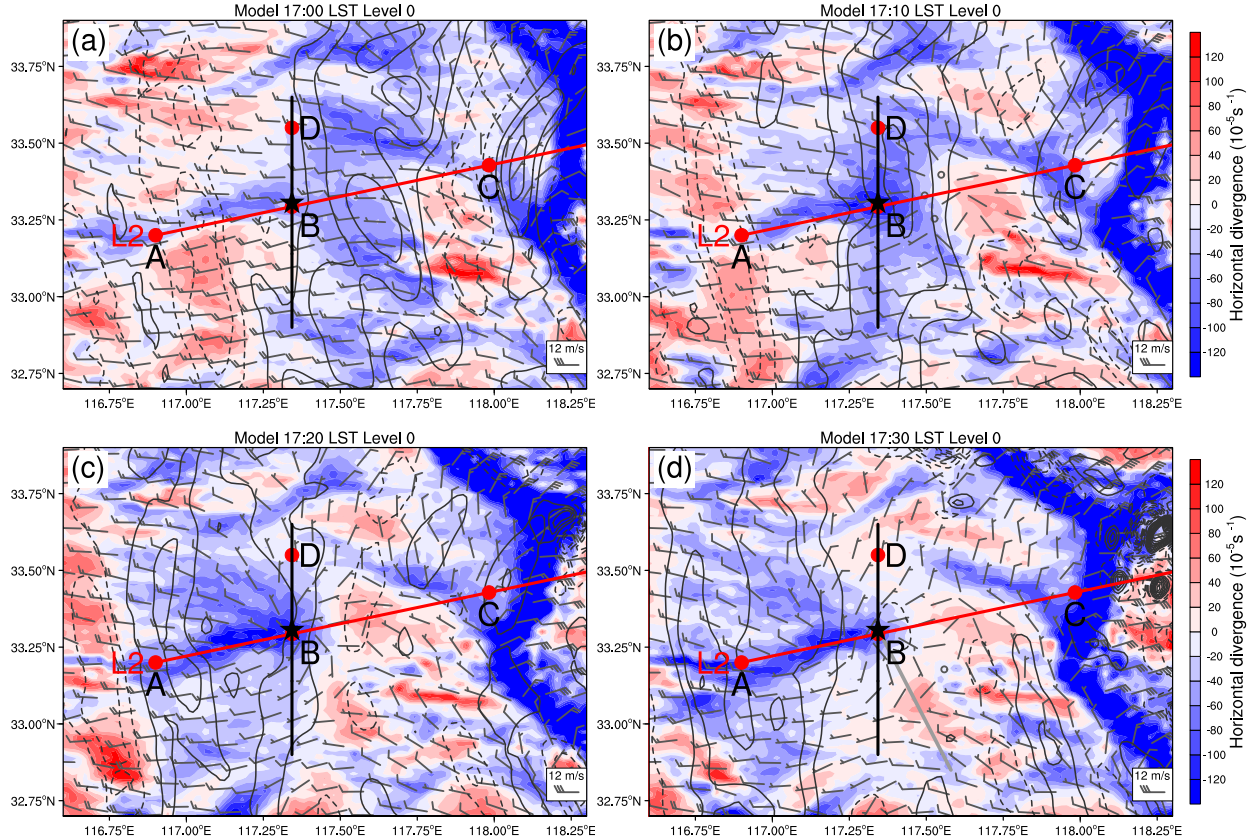


FIG. 13. Horizontal divergence (shaded, 10^{-5} s^{-1}), wind fields (full and half barbs represent 4 and 2 m s^{-1} , respectively) on the bottom level of WRF output, and vertical velocity (black contours with 0.5 m s^{-1} intervals, dashed for negative values) at 6-km height of WRF output at (a) 1700, (b) 1710, (c) 1720, and 1730 LST.

5. Structure of gravity waves and their roles in CI

a. Vertical structure of the gravity wave and CI processes

The updraft forced by the low-level horizontal convergence line is shown by the north–south-oriented vertical cross section through CI location B (Fig. 14). The updraft was confined below 3 km, with maximum upward vertical velocity at 1.5 km (Fig. 14a). The divergence zone at 3 km corresponded with the low-level convergence zone and the updraft. The LFC and LCL were both slightly higher than 3 km. Therefore, the low-level confined updraft corresponding to the convergence line can hardly lift the air parcel above LCL unless there is disturbance. Other cross sections normal to the convergence line also show such features before the gravity wave arrived (not shown), suggesting homogeneous characteristics along the convergence line. As the convergence zone of the divergence–convergence couplet approached the cross section at 1710 LST (Fig. 13b), the updraft and the convergence extended substantially (Fig. 14b). After 10 min, the strengthened updraft

initiated a cloud above the LFC at 1720 LST (Fig. 14c). At 1730 LST, the cloud was developing rapidly when the updraft and convergence caused by the gravity wave weakened (Fig. 14d).

Figures 15 and 16 show the vertical structure and the propagation of the gravity wave by using time–height plots of locations A, B, C, and D in Fig. 13. When the convergence zone of the surface divergence–convergence couplets passed the CI location B at approximately 1700–1730 LST (Figs. 13 and 14), the enhancement of the updraft can also be seen in Fig. 15b. The updraft caused by the gravity wave had a maximal upward vertical velocity at ~ 6 km, suggesting the gravity wave to be an $n = 1$ mode gravity wave whose vertical wavelength is twice the depth of the troposphere. This upper-level updraft has a similar horizontal divergence feature with the low-level updraft, both of which are characterized by convergence in the lower half depth of the updraft and divergence in the upper half depth of the updraft (Fig. 16b). Similarly, the downdraft is characterized by divergence in the lower half depth of the downdraft and convergence in the upper half depth of the downdraft. It should be noted that the divergence

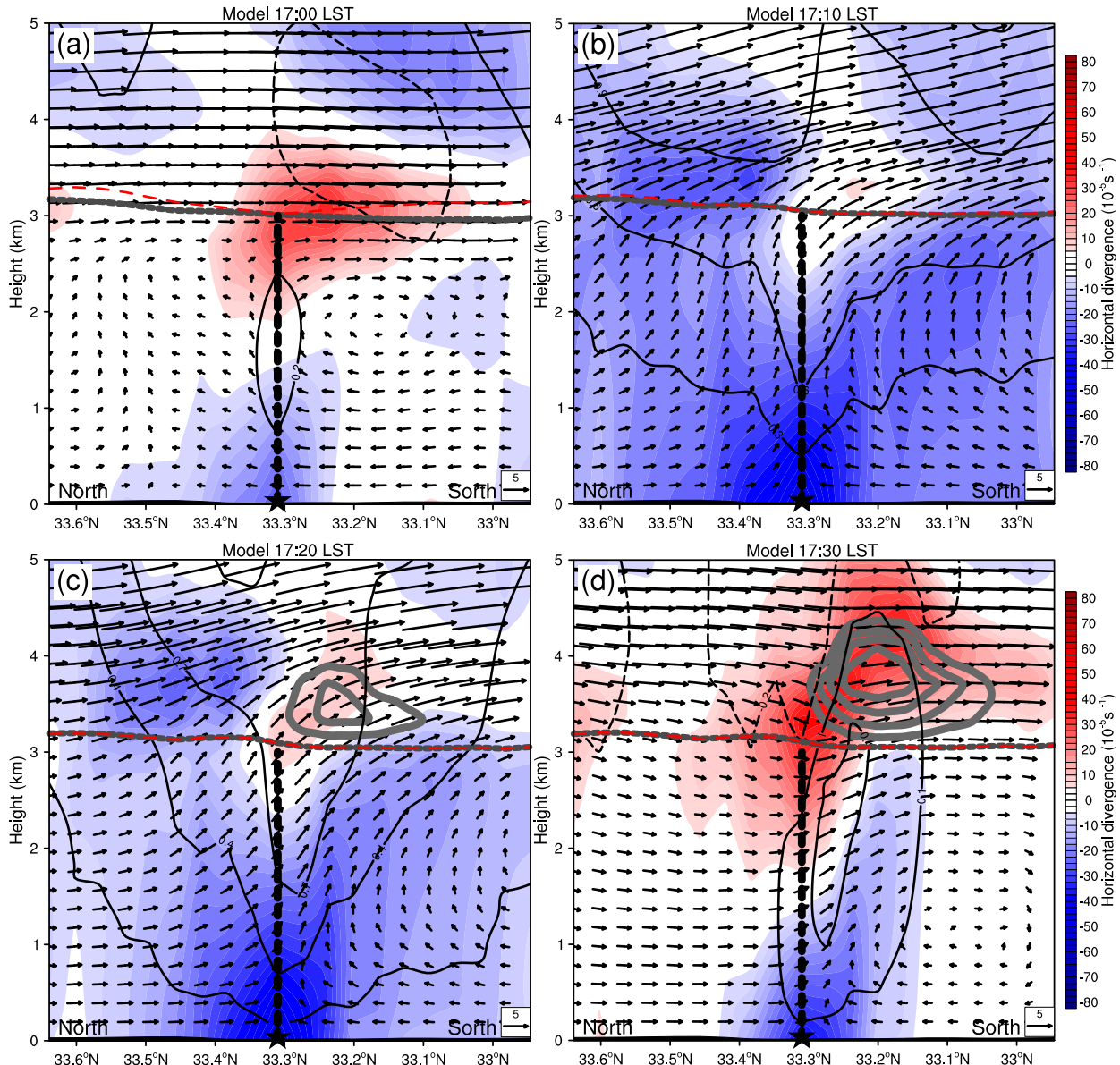


FIG. 14. Vertical cross sections along the north–south-oriented black lines in Fig. 13 at (a) 1700, (b) 1710, (c) 1720, and 1730 LST. Plots are horizontal divergence (shaded, 10^{-5} s^{-1}), wind vectors, vertical velocity (black contours with 0.3 m s^{-1} intervals, dashed for negative values), and cloud water mixed ratio (gray contours, g kg^{-1}). The vertical thick dashed lines denote the position and height of low-level convergence line. The horizontal dashed lines are the height of LCL (gray lines) and LFC (red lines). The black stars denote the location of the strongest updraft that initiated Cb (i.e., the CI location of Cb).

field in Fig. 16b is the composition of the low-level divergence features related to the updraft below 3 km and the deep tropospheric divergence features related to the downdraft-updraft couplets of $n = 1$ waves, whereas the divergence time–height plot at location D (north of the low-level convergence line) shows the divergence feature caused only by the $n = 1$ wave (Fig. 16d).

The simulated surface features related to the gravity wave are shown in Figs. 15 and 16. In the model, besides the pressure dip of the wave that initiated Cb (denoted

by W2), a weaker pressure dip (denoted by W1) and several perturbations are also identifiable. Figures 15a and 15b show that it took the pressure dip ~ 25 min to propagate across 42.4 km (from B to A in Fig. 13); thus, a wave speed of $\sim 28.3 \text{ m s}^{-1}$ is calculated. The speed is consistent with observations in section 3b and ASJ13 considering errors. The polarization relation of ducted gravity waves, which indicates the sinking (rising) motion and adiabatic warming (cooling) leads (trails) the surface pressure minimum by a quarter wavelength of

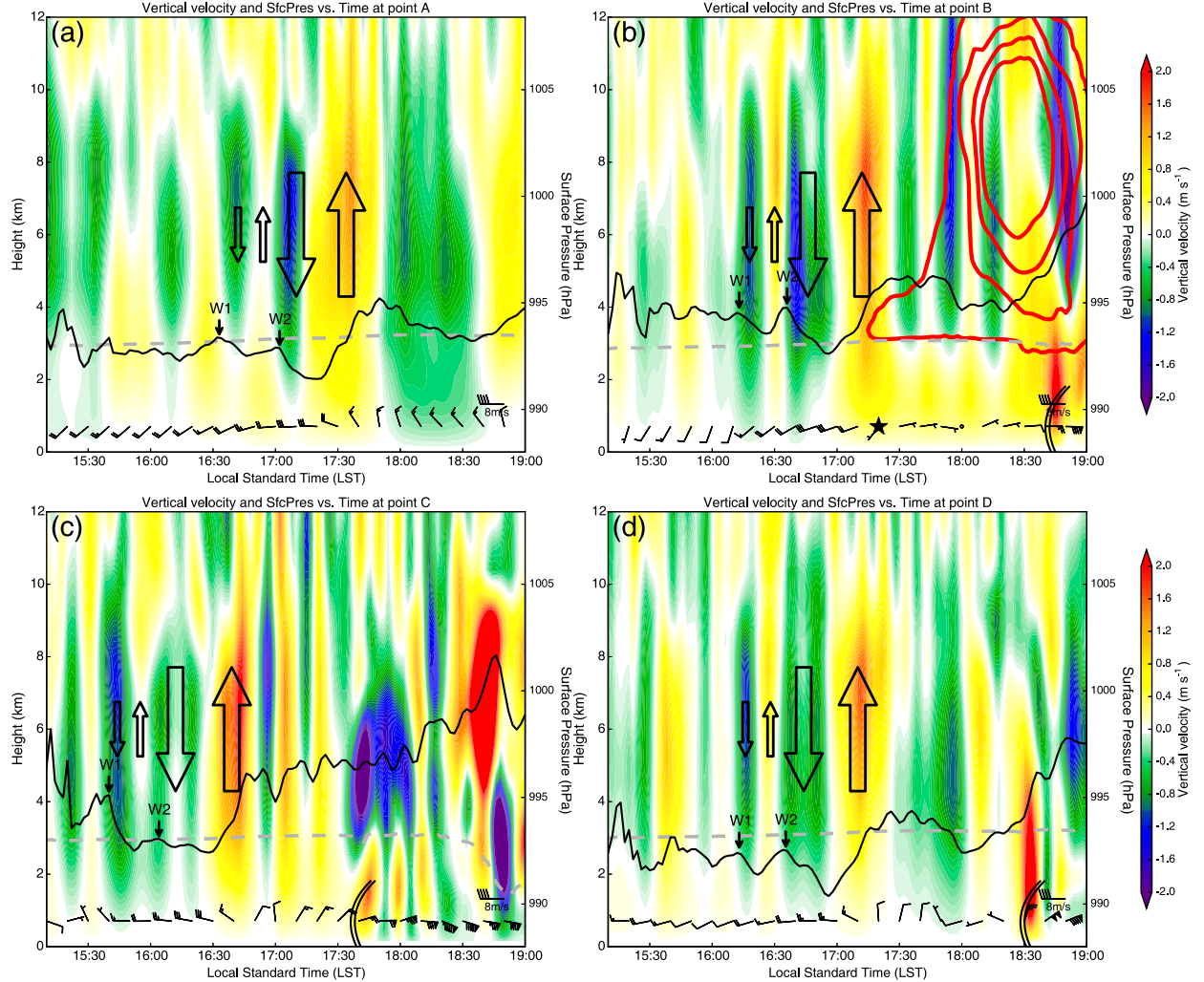


FIG. 15. Time–height plots of simulated vertical velocity (shaded, m s^{-1}) and LCL (dashed gray lines) at point (a) A, (b) B, (c) C, and (d) D, whose locations are marked by red dots in Fig. 13. Red contours in (b) are hydrometeor values starting at 1 g kg^{-1} by increments of 20 g kg^{-1} . Time series of simulated surface pressure at these locations are overlaid, with a second y axis on the right. Time series of surface wind barbs (full and half barbs represent 2 and 1 m s^{-1} , respectively) are shown at the bottom. The hollow arrows indicate the updraft–downdraft couplets. Two pressure dips discussed in the text are denoted by W1 and W2, respectively.

the gravity waves (see the schematic in Fig. 20a), is shown in these waves by comparing the time series of surface pressure and vertical velocity in Fig. 15. Also evident is that the wave of depression (wave W2) is not symmetrical, which is characterized by a larger pressure rise than the pressure fall in the surface pressure dip. This suggests a stronger updraft than the downdraft of the $n = 1$ wave because the surface pressure rise (fall) is caused by the updraft (downdraft) of the wave. The net effect of the wave is a permanent upward displacement and rise of surface pressure compared to the original state before the wave passes. This net rise of surface pressure leads to the veering of the surface wind to the propagating direction of the wave, whereas the surface wind returns to its original state for a symmetrical wave.

Therefore, in the observations, the wind veering to the direction of the wave also suggested a net positive upward displacement caused by the $n = 1$ wave.

The $n = 1$ gravity wave, which has an updraft stronger than the downdraft, is supposed to have a positive net contribution to Cb's initiation. However, the widespread wave did not trigger convection elsewhere along its path in the model. This suggests the $n = 1$ wave alone was not sufficient to trigger convection in this case. The low-level updraft corresponding to the convergence line was also insufficient to trigger convection alone. The convection was only initiated at their intersection, where the updrafts were combined and strengthened. Comparing Fig. 15a with Fig. 15b and Fig. 16a with Fig. 16b, it can be seen that as the $n = 1$ wave continued to

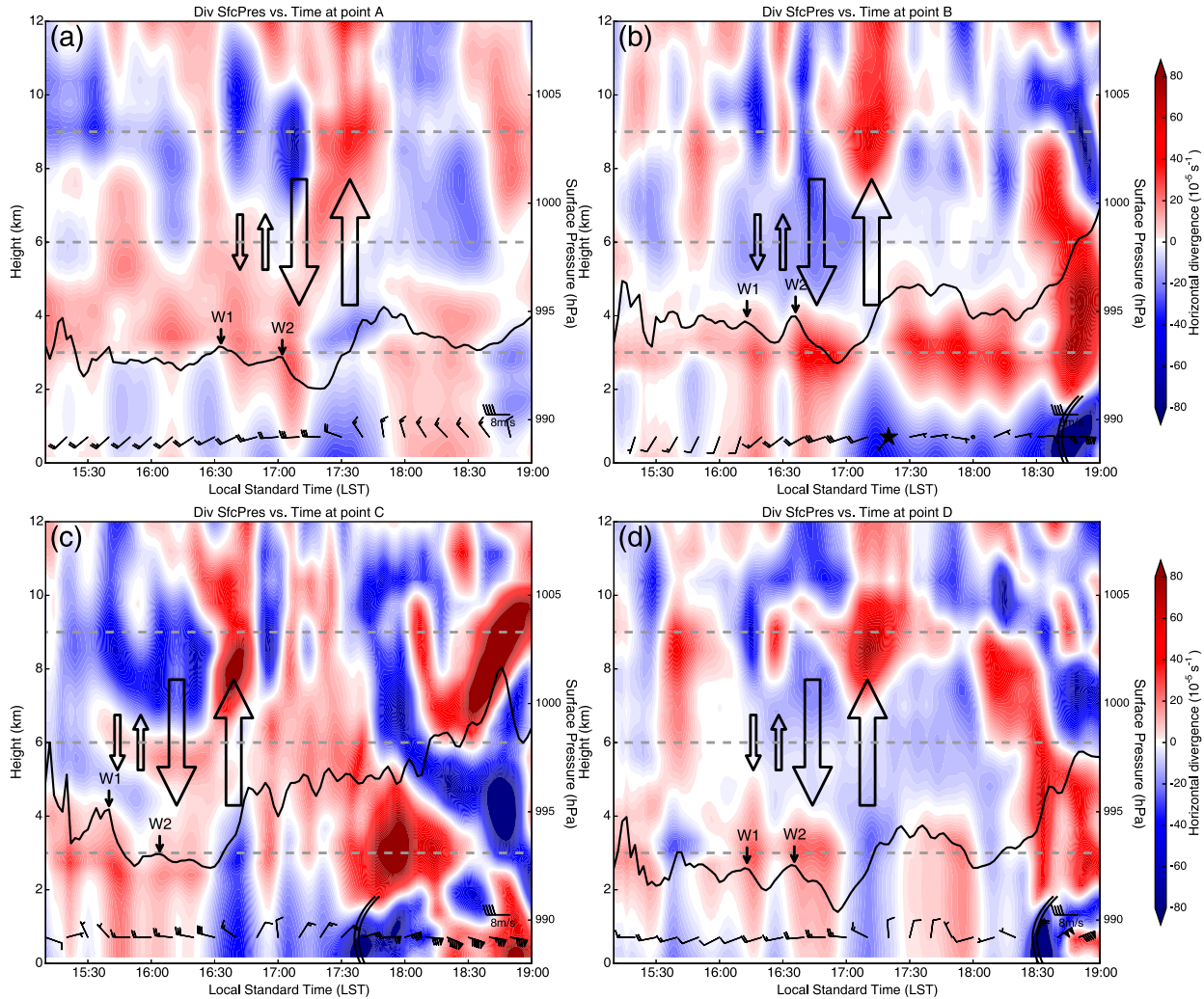


FIG. 16. As in Fig. 15, but with horizontal divergence (shaded, s^{-1}). The dashed gray lines mark the height of 3, 6, and 9 km, respectively.

propagate, the gravity wave became weaker, as indicated by the weaker updraft and weaker convergence. Therefore, the convection was only initiated at the eastern end of the convergence line where the gravity wave was still strong enough.

To further investigate the vertical features and the excitation of the gravity waves, vertical cross sections along the propagating direction of the gravity waves are shown (Fig. 17). The cross sections pass through the earlier convection source so that the generation process of the wave can be examined. In addition to the downdraft-updraft couplets (hollow arrows in Figs. 17c and 17d) and the related divergence features (Fig. 17d), which are consistent with the features described by Figs. 15 and 16, the cross section at 1552 LST also shows a strong easterly flow at a height ~ 9 km (Fig. 17c). The upper-level easterly flow came from the outflow of the earlier convection (hollow arrows in Fig. 17a). The

outflow owing to the convective updraft caused the convergence zone at its leading edge, resulting in subsidence beneath the outflow (Fig. 17b). This subsidence propagating westward with the upper-level easterly flow later evolved into the $n = 1$ gravity wave circulation (Fig. 17d). Previous studies have noted that diabatic heating and nonlinear sources within the cloud are important for wave generation by convection (e.g., Beres et al. 2004; Lane et al. 2001; Song et al. 2003; Stephan et al. 2016); while in this case, it appears that the nonlinearity caused by the upper-level outflow outside the cloud also plays an important role in the $n = 1$ wave generation. This should be comparable to the well-known transition between bores and solitary waves in boundary layers; furthermore, high-order waves ($n = 2$, $n = 3$, etc.) are unlikely to be generated in this way. The upper-level outflow can be identified in visible satellite images as cirrus anvil (e.g., Fig. 5a; Fig. 6 in BP10).

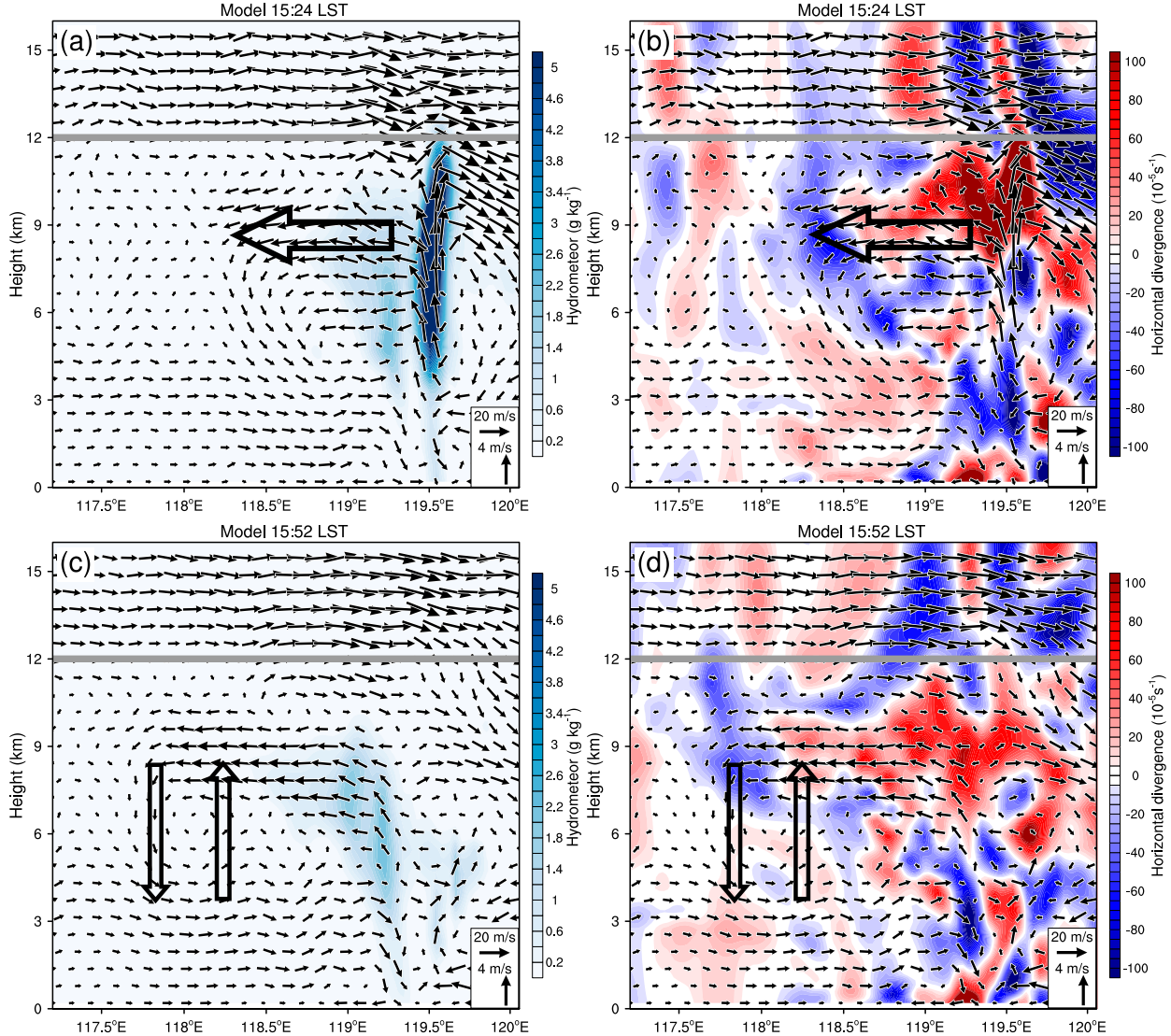


FIG. 17. Vertical cross sections of hydrometeor (left shaded, g kg^{-1}) and horizontal divergence (right shaded, s^{-1}) with wind vectors projected to the cross section along L1 (position is shown in Fig. 10) at (a), (b) 1524 and (c), (d) 1552 LST 5 Jun 2009. The horizontal arrows indicate the outflows of convection, while the vertical arrows indicate the updraft–downdraft couples of the gravity wave. The height of 12 km is marked by thick gray lines.

Therefore, in deep convection cases, in which there are outflow anvils on high-resolution visible satellite images, $n = 1$ gravity waves can be anticipated, which could be useful in predicting the timing of CI when other datasets are not sufficiently dense. We note that the wave generation mechanism is much more complex than what has been shown here and needs further studying, especially by using quantitative methods and nonlinear models such as WRF.

b. CI environments

Figure 18 shows the model-derived sounding time series at the starred CI location. The 1400 LST sounding (gray lines) is shown to describe the pre-CI environment

that had not been affected by gravity waves. The figure shows a moist layer at the 700-hPa level and a dry layer at the 500-hPa level at 1400 LST. The midlevel features are comparable to the sounding at Fuyang station (Fig. 4c) since the CI location was also behind the 500-hPa trough by this time. Note that as the ground temperature rose in the afternoon, the inversion below 850 hPa at 0800 LST was eliminated due to surface heating. The lapse rate below 700 hPa became nearly equal to the dry air adiabatic lapse rate, which indicates that the low-level atmosphere was well mixed.

Soundings of three other times (Fig. 18) at 1700 LST (light blue lines), 1710 LST (blue lines), and 1720 LST

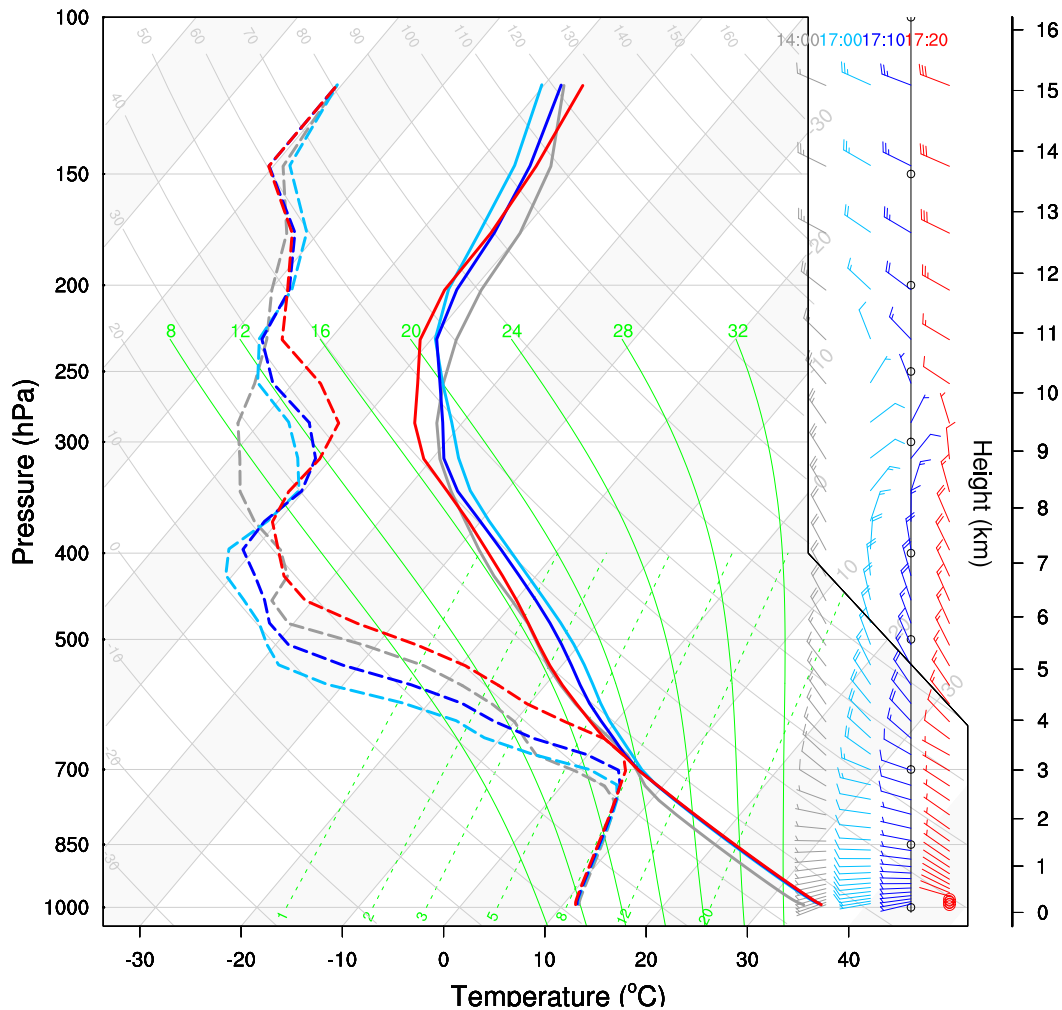


FIG. 18. Simulated sounding time series of dewpoint temperature (dashed lines), temperature (solid lines), and wind profiles from the model starred CI location (shown in Fig. 13) at 1400 (gray), 1700 (light blue), 1710 (blue), and 1720 (red) LST 5 Jun 2009.

(red lines) show how the environments were modified when the updraft of the gravity wave passed the CI location during 1700–1720 LST (Fig. 13). The temperature stayed the same below the 700-hPa level but the temperature between the 700- and 250-hPa level dropped quickly and simultaneously during the 20 min when the gravity wave passed by. As the temperature dropped, the dewpoint temperature lines shifted in parallel. These changes corresponded to the deep-layer upward motion of the $n = 1$ wave. The cooling in the middle troposphere results in more unstable conditions for convection. Though the upward motion cannot be shown by the stationary temperature profile in the mixed layer below 700 hPa, the dewpoint temperature profile showed that the moist layer at the 700-hPa level was quickly lifted as the wave passed. The lifted moist layer became saturated by 1720 LST, when the convection cell was initiated.

BP10 observed warming between 800 and 900 hPa and cooling at midlevels by successively released soundings in prestorm environment with about 30-min time intervals (see their Fig. 8c). They attribute the warming to the subsidence of an $n = 1$ mode gravity wave but the midlevel cooling could also be attributed to the $n = 1$ wave. Considering the temperature does not change if the lapse rate is equal to the dry adiabatic lapse rate, this explains why only part of the uplifting atmosphere was cooling notably. It should be noted that since it takes about 20 min for the radiosonde to ascend to 500 hPa and even more time to ascend higher, and the $n = 1$ wave can propagate to long distances in 20 min; thus, it is probably that the observed soundings in **BP10** captured the features of the subsidence at the beginning and the uplifting at the later time. This indicates that more advanced sounding technologies are needed for the observational study of $n = 1$ waves.

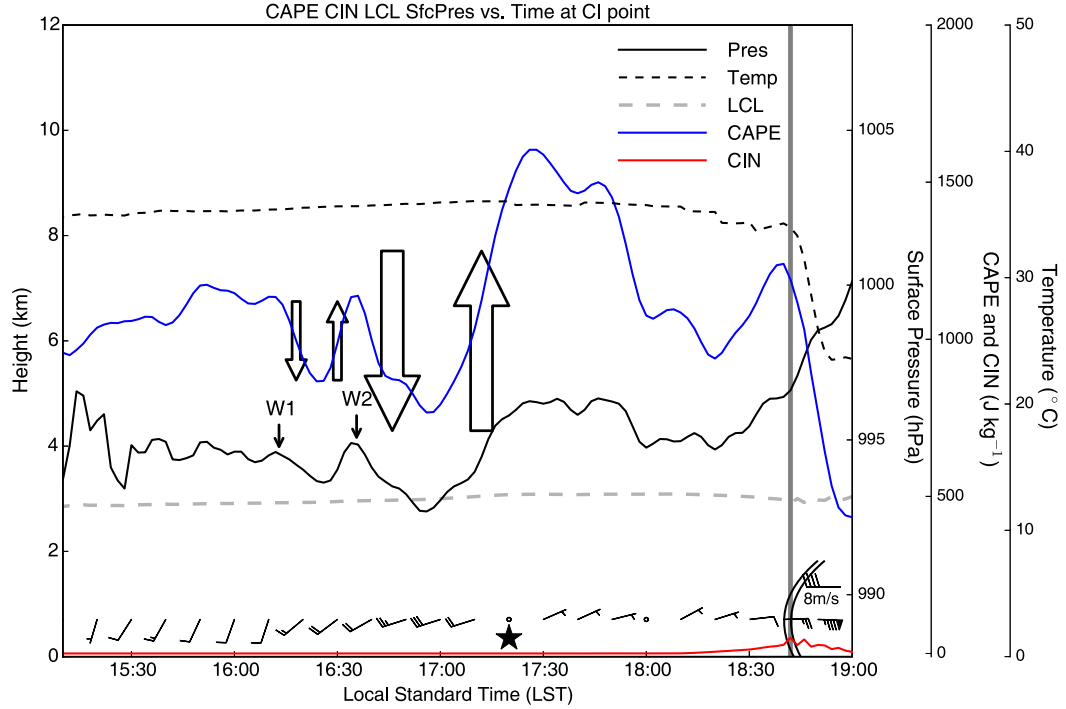


FIG. 19. As in Fig. 15, but with the time series of CAPE (blue line), CIN (red line), temperature (black dashed line), and LCL (gray dashed line). The black star indicates the time of CI. The vertical gray line indicates the arrival of gust front.

Figure 19 shows the variations of the stability parameters at the same CI location. The temperature was around 35°C until the gust front arrived after 1840 LST, which is consistent with the surface observations (e.g., Fig. 6b). The LCL was about 3 km high at all times, regardless of the disturbance of the gravity wave. The CIN near the CI location was close to zero during this case. The CAPE varied corresponding to the surface pressure before the gust front arrived. They both changed owing to the deep $n = 1$ waves. The subsidence warming reduced the CAPE and the surface pressure, whereas the cooling from the upward motion increased the CAPE and the surface pressure. At 1720 LST, the CAPE rose even higher than the values before the gravity waves passed by. The higher CAPE value facilitated the development of convection. However, this was also a consequence of the gravity waves and not the primary reason for CI. A CAPE value about 1000 J kg^{-1} combined with the absence of CIN should be sufficient to support CI under general circumstances.

6. Summary

This study documents the 5 June 2009 severe convection event in which gravity wave played an important role in CI. Surface features of the gravity wave,

including a pressure dip and a wind shift in advance of a gust front, were observed using high-frequency automatic weather station (AWS) data. The pressure dip was similar to the previously observed $n = 1$ mode gravity waves by ASJ13. However, the wind shift accompanied by the pressure dip, which was caused by $n = 1$ wave, was not noted in their study. Several convective cloud systems occurred during this case, among which the cloud feature Cb (Fig. 5) was specifically focused on. Cb developed intensely after CI and brought severe surface wind that resulted in 25 deaths in Anhui. It was found the initiation of Cb was influenced by the gravity wave.

AWS data, visible satellite data, and Doppler radar data were combined to show the initiation and development of convection. Observations show two precursors to the cloud feature Cb's initiation (Fig. 5), including a quasi-stationary west–east-oriented convergence line and a sudden wind shift at the eastern end of the convergence line. High-resolution WRF simulation was used to examine the structure of the gravity waves and forecast CI processes. The model reproduced the observed surface precursors to Cb's initiation and observed features of the gravity wave, and the three-dimensional model output was further analyzed.

Based on the polarization relationship of ducted gravity wave, the primary features of the $n = 1$ gravity

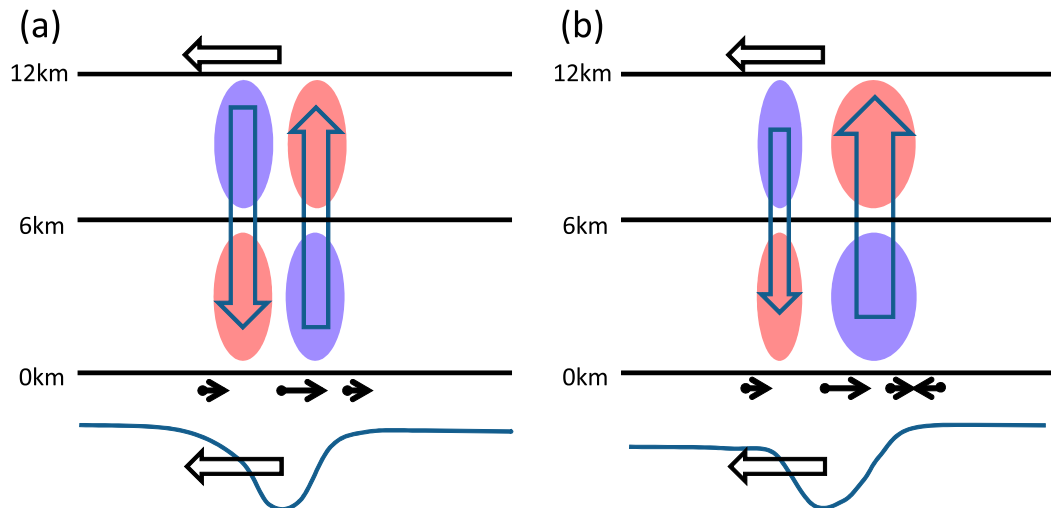


FIG. 20. Schematic picture of the vertical cross section of $n = 1$ gravity waves propagating toward the left. Blue hollow arrows indicate the downdraft-updraft couplets. The solid blue curves represent the changes of surface pressure. The horizontal black arrows represent the changes of surface winds. The shaded ellipses represent the divergence fields corresponding to the vertical motion (blue indicates convergence, red indicates divergence). Plots are (a) a symmetrical wave and (b) a wave that has a stronger updraft than downdraft.

wave are shown in Fig. 20a. The updraft (downdraft) corresponds to divergence (convergence) in the upper half of the troposphere and convergence (divergence) in the lower half of the troposphere. The pressure dip at the surface propagates with the $n = 1$ wave. The surface wind and pressure return to their original state after the wave passes. In this study, the $n = 1$ wave that contributes to CI (Fig. 20b) is characterized by updraft stronger than the downdraft. The net effects of this wave are upward air displacement, a rise in pressure, and a wind shift toward the direction of the wave. The existence of this wave in this case is supported by surface observations and the upward displacement of the wave led to Cb's initiation.

Figure 21 summarizes the processes related to the $n = 1$ gravity wave and CI. The approximately west–east-oriented convergence line (Fig. 21a) helped focus the initiation of cloud features Ca and Cb (Figs. 2 and 5). However, cloud feature Ca, which occurred near the west edge of the convergence line, did not evolve into deep convection. The coastal deep convective generated $n = 1$ gravity waves as well as gust fronts that propagated toward the convergence line. The leading outflow edge of cloud feature C1 (Fig. 2) corresponded to the subsidence of the $n = 1$ wave and was at least partially responsible for the generation of the wave. This provides implications for exploring prestorm environments of squall lines and can reasonably explain the pressure drop ahead of the anvil observed by BP10.

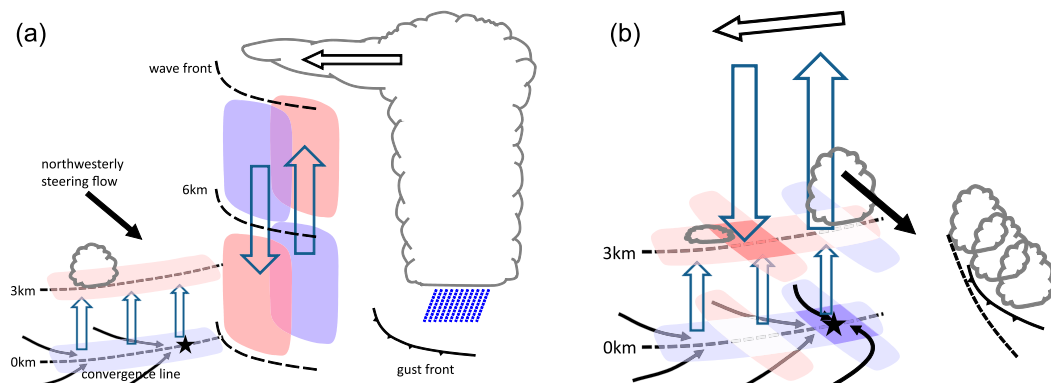


FIG. 21. Schematic pictures of $n = 1$ gravity wave and CI processes. The blue and red colors are as in Fig. 20. (a) The generation of $n = 1$ gravity wave and the vertical structure of the convergence line, and (b) the intersection between the $n = 1$ wave and the convergence line and the surface wind shifts.

When the $n = 1$ wave intersected with the convergence line (Fig. 21b), the updraft of the wave strengthened the updraft confined below the 3-km height that was forced by the surface convergence line. The strengthened updraft led to Cb's initiation, whereas Ca weakened correspondingly. The divergence features of the surface and 3 km are also shown in Fig. 21. Cb was initiated at the area marked by the star, where the maximum surface convergence and the strongest updraft occurred. The west–east-oriented belt of convergence on the surface was formed by the convergence line, whereas the convergence belt normal to the west–east-oriented convergence line was caused by the $n = 1$ wave. The sudden wind veering at the eastern end of the convergence line was also caused by the $n = 1$ wave. The gust front that was left behind by the $n = 1$ wave intersected with the north–south-oriented convergence line indicated by a shallow cloud line and initiated C3. The type of C3's initiation is well documented by previous studies.

This study provides a new type of along-line variability of updraft as the trigger mechanism of CI, which is caused by the intersection of a convergence line and a gravity wave. The positive contribution of $n = 1$ gravity waves to CI has not been documented before. The $n = 1$ wave with stronger updraft than downdraft that helped trigger Cb was generated at the decaying stage of C1 when the gust front was also generated. We speculate that it may be attributed to the weakening heating profile or the additional effect of the rainfall inside the convection cell, which needs further investigation in the future.

Acknowledgments. This work was primarily supported by the National Fundamental Research 973 Program of China (2013CB430104). We thank the Key Lab of Mesoscale Severe Weather/Ministry of Education of China (in Nanjing University) for collecting and providing the mesoscale dataset (automatic weather station data, radar, and satellite data) and the JMA reanalysis data. We are grateful to the editor (Dr. Lane) and three anonymous reviewers for their thorough reviews that helped improve the manuscript.

REFERENCES

- Adams-Selin, R. D., and R. H. Johnson, 2010: Mesoscale surface pressure and temperature features associated with bow echoes. *Mon. Wea. Rev.*, **138**, 212–227, doi:10.1175/2009MWR2892.1.
- , and —, 2013: Examination of gravity waves associated with the 13 March 2003 bow echo. *Mon. Wea. Rev.*, **141**, 3735–3756, doi:10.1175/MWR-D-12-00343.1.
- Atkins, N. T., R. M. Wakimoto, and T. M. Weckwerth, 1995: Observations of the sea-breeze front during CaPE. Part II: Dual-Doppler and aircraft analysis. *Mon. Wea. Rev.*, **123**, 944–969, doi:10.1175/1520-0493(1995)123<0944:OTSBF>2.0.CO;2.
- Beres, J. H., M. J. Alexander, and J. R. Holton, 2004: A method of specifying the gravity wave spectrum above convection based on latent heating properties and background wind. *J. Atmos. Sci.*, **61**, 324–337, doi:10.1175/1520-0469(2004)061<0324:AMOSTG>2.0.CO;2.
- Birch, C. E., D. J. Parker, A. O'Leary, J. H. Marsham, C. M. Taylor, P. P. Harris, and G. M. S. Lister, 2013: Impact of soil moisture and convectively generated waves on the initiation of a West African mesoscale convective system. *Quart. J. Roy. Meteor. Soc.*, **139**, 1712–1730, doi:10.1002/qj.2062.
- Bretherton, C. S., and P. K. Smolarkiewicz, 1989: Gravity waves, compensating subsidence and detrainment around cumulus clouds. *J. Atmos. Sci.*, **46**, 740–759, doi:10.1175/1520-0469(1989)046<0740:GWCSAD>2.0.CO;2.
- Browning, K. A., and Coauthors, 2007: The Convective Storm Initiation Project. *Bull. Amer. Meteor. Soc.*, **88**, 1939–1955, doi:10.1175/BAMS-88-12-1939.
- Bryan, G. H., and M. D. Parker, 2010: Observations of a squall line and its near environment using high-frequency rawinsonde launches during VORTEX2. *Mon. Wea. Rev.*, **138**, 4076–4097, doi:10.1175/2010MWR3359.1.
- , J. C. Wyngaard, and J. M. Fritsch, 2003: Resolution requirements for the simulation of deep moist convection. *Mon. Wea. Rev.*, **131**, 2394–2416, doi:10.1175/1520-0493(2003)131<2394:RRFTSO>2.0.CO;2.
- Chen, F., and J. Dudhia, 2001: Coupling an advanced land surface-hydrology model with the Penn State–NCAR MM5 modeling system. Part I: Model implementation and sensitivity. *Mon. Wea. Rev.*, **129**, 569–585, doi:10.1175/1520-0493(2001)129<0569:CAALSH>2.0.CO;2.
- Crook, N. A., 1996: Sensitivity of moist convection forced by boundary layer processes to low-level thermodynamic fields. *Mon. Wea. Rev.*, **124**, 1767–1785, doi:10.1175/1520-0493(1996)124<1767:SMOCFB>2.0.CO;2.
- Ding, Y., 1992: A study on the formation condition of squall line in China (in Chinese). *Chin. J. Atmos. Sci.*, **6**, 18–27.
- Dudhia, J., 1989: Numerical study of convection observed during the winter monsoon experiment using a mesoscale two-dimensional model. *J. Atmos. Sci.*, **46**, 3077–3107, doi:10.1175/1520-0469(1989)046<3077:NSOCOD>2.0.CO;2.
- Fovell, R. G., 2002: Upstream influence of numerically simulated squall-line storms. *Quart. J. Roy. Meteor. Soc.*, **128**, 893–912, doi:10.1256/0035900021643737.
- , G. L. Mullendore, and S.-H. Kim, 2006: Discrete propagation in numerically simulated nocturnal squall lines. *Mon. Wea. Rev.*, **134**, 3735–3752, doi:10.1175/MWR3268.1.
- Fritsch, J. M., and R. E. Carbone, 2004: Improving quantitative precipitation forecasts in the warm season: A USWRP research and development strategy. *Bull. Amer. Meteor. Soc.*, **85**, 955–965, doi:10.1175/BAMS-85-7-955.
- Hane, C. E., R. M. Rabin, T. M. Crawford, H. B. Bluestein, and M. E. Baldwin, 2002: A case study of severe storm development along a dryline within a synoptically active environment. Part II: Multiple boundaries and convective initiation. *Mon. Wea. Rev.*, **130**, 900–920, doi:10.1175/1520-0493(2002)130<0900:ACSOSS>2.0.CO;2.
- Hong, S.-Y., and J.-O. J. Lim, 2006: The WRF single-moment 6-class microphysics scheme (WSM6). *J. Korean Meteor. Soc.*, **42**, 129–151.
- , Y. Noh, and J. Dudhia, 2006: A new vertical diffusion package with an explicit treatment of entrainment processes. *Mon. Wea. Rev.*, **134**, 2318–2341, doi:10.1175/MWR3199.1.
- Iacono, M. J., J. S. Delamere, E. J. Mlawer, M. W. Shephard, S. A. Clough, and W. D. Collins, 2008: Radiative forcing by

- long-lived greenhouse gases: Calculations with the AER radiative transfer models. *J. Geophys. Res.*, **113**, D13103, doi:[10.1029/2008JD009944](https://doi.org/10.1029/2008JD009944).
- Jacques, A. A., J. D. Horel, E. T. Crosman, and F. L. Vernon, 2015: Central and eastern U.S. surface pressure variations derived from the USArray network. *Mon. Wea. Rev.*, **143**, 1472–1493, doi:[10.1175/MWR-D-14-00274.1](https://doi.org/10.1175/MWR-D-14-00274.1).
- Kain, J. S., 2004: The Kain–Fritsch convective parameterization: An update. *J. Appl. Meteor.*, **43**, 170–181, doi:[10.1175/1520-0450\(2004\)043<0170:TKCPAU>2.0.CO;2](https://doi.org/10.1175/1520-0450(2004)043<0170:TKCPAU>2.0.CO;2).
- Kingsmill, D. E., 1995: Convection initiation associated with a sea-breeze front, a gust front, and their collision. *Mon. Wea. Rev.*, **123**, 2913–2933, doi:[10.1175/1520-0493\(1995\)123<2913:CIAWAS>2.0.CO;2](https://doi.org/10.1175/1520-0493(1995)123<2913:CIAWAS>2.0.CO;2).
- Koch, S. E., and J. McCarthy, 1982: The evolution of an Oklahoma dryline. Part II: Boundary-layer forcing of mesoconvective systems. *J. Atmos. Sci.*, **39**, 237–257, doi:[10.1175/1520-0469\(1982\)039<0237:TEOAOD>2.0.CO;2](https://doi.org/10.1175/1520-0469(1982)039<0237:TEOAOD>2.0.CO;2).
- , and W. L. Clark, 1999: A nonclassical cold front observed during COPS-91: Frontal structure and the process of severe storm initiation. *J. Atmos. Sci.*, **56**, 2862–2890, doi:[10.1175/1520-0469\(1999\)056<2862:ANCFOD>2.0.CO;2](https://doi.org/10.1175/1520-0469(1999)056<2862:ANCFOD>2.0.CO;2).
- Lac, C., J. P. Lafore, and J. L. Redelsperger, 2002: Role of gravity waves in triggering deep convection during TOGA COARE. *J. Atmos. Sci.*, **59**, 1293–1316, doi:[10.1175/1520-0469\(2002\)059<1293:ROGWIT>2.0.CO;2](https://doi.org/10.1175/1520-0469(2002)059<1293:ROGWIT>2.0.CO;2).
- Lane, T. P., and M. J. Reeder, 2001: Convectively generated gravity waves and their effect on the cloud environment. *J. Atmos. Sci.*, **58**, 2427–2440, doi:[10.1175/1520-0469\(2001\)058<2427:CGGWAT>2.0.CO;2](https://doi.org/10.1175/1520-0469(2001)058<2427:CGGWAT>2.0.CO;2).
- , and F. Zhang, 2011: Coupling between gravity waves and tropical convection at mesoscales. *J. Atmos. Sci.*, **68**, 2582–2598, doi:[10.1175/2011JAS3577.1](https://doi.org/10.1175/2011JAS3577.1).
- , and M. W. Moncrieff, 2015: Long-lived mesoscale systems in a low-convective inhibition environment. Part I: Upshear propagation. *J. Atmos. Sci.*, **72**, 4297–4318, doi:[10.1175/JAS-D-15-0073.1](https://doi.org/10.1175/JAS-D-15-0073.1).
- , M. J. Reeder, and T. L. Clark, 2001: Numerical modeling of gravity wave generation by deep tropical convection. *J. Atmos. Sci.*, **58**, 1249–1274, doi:[10.1175/1520-0469\(2001\)058<1249:NMOGWG>2.0.CO;2](https://doi.org/10.1175/1520-0469(2001)058<1249:NMOGWG>2.0.CO;2).
- Locatelli, J. D., M. T. Stoelinga, P. V. Hobbs, and J. Johnson, 1998: Structure and evolution of an undular bore on the high plains and its effects on migrating birds. *Bull. Amer. Meteor. Soc.*, **79**, 1043–1060, doi:[10.1175/1520-0477\(1998\)079<1043:SAEOAU>2.0.CO;2](https://doi.org/10.1175/1520-0477(1998)079<1043:SAEOAU>2.0.CO;2).
- Mapes, B. E., 1993: Gregarious tropical convection. *J. Atmos. Sci.*, **50**, 2026–2037, doi:[10.1175/1520-0469\(1993\)050<2026:GTC>2.0.CO;2](https://doi.org/10.1175/1520-0469(1993)050<2026:GTC>2.0.CO;2).
- May, P. T., 1999: Thermodynamic and vertical velocity structure of two gust fronts observed with a wind profiler/RASS during MCTEX. *Mon. Wea. Rev.*, **127**, 1796–1807, doi:[10.1175/1520-0493\(1999\)127<1796:TAVVSO>2.0.CO;2](https://doi.org/10.1175/1520-0493(1999)127<1796:TAVVSO>2.0.CO;2).
- Meng, Z., D. Yan, and Y. Zhang, 2013: General features of squall lines in East China. *Mon. Wea. Rev.*, **141**, 1629–1647, doi:[10.1175/MWR-D-12-00208.1](https://doi.org/10.1175/MWR-D-12-00208.1).
- Murphrey, H. V., R. M. Wakimoto, C. Flamant, and D. E. Kingsmill, 2006: Dryline on 19 June 2002 during IHOP. Part I: Airborne Doppler and LEANDRE II analyses of the thin line structure and convection initiation. *Mon. Wea. Rev.*, **134**, 406–430, doi:[10.1175/MWR3063.1](https://doi.org/10.1175/MWR3063.1).
- Nicholls, M. E., R. A. Pielke, and W. R. Cotton, 1991: Thermally forced gravity waves in an atmosphere at rest. *J. Atmos. Sci.*, **48**, 1869–1884, doi:[10.1175/1520-0469\(1991\)048<1869:TFGWIA>2.0.CO;2](https://doi.org/10.1175/1520-0469(1991)048<1869:TFGWIA>2.0.CO;2).
- NPD/JMA, 1997: Outline of the operational numerical weather prediction of the Japan Meteorological Agency. Appendix to WMO Tech. Progress Rep. on the Global Data Processing and Forecasting System and Numerical Weather Prediction, Numerical Prediction Division, Department of Forecast, Japan Meteorological Agency, 48–63. [Available online at <http://www.jma.go.jp/jma/jma-eng/jma-center/nwp/nwp-top.htm>.]
- Pandya, R. E., and D. R. Durran, 1996: The influence of convectively generated thermal forcing on the mesoscale circulation around squall lines. *J. Atmos. Sci.*, **53**, 2924–2951, doi:[10.1175/1520-0469\(1996\)053<2924:TIOCGT>2.0.CO;2](https://doi.org/10.1175/1520-0469(1996)053<2924:TIOCGT>2.0.CO;2).
- Purdom, J. F. W., 1976: Some uses of high-resolution GOES imagery in the mesoscale forecasting of convection and its behavior. *Mon. Wea. Rev.*, **104**, 1474–1483, doi:[10.1175/1520-0493\(1976\)104<1474:SUOHRG>2.0.CO;2](https://doi.org/10.1175/1520-0493(1976)104<1474:SUOHRG>2.0.CO;2).
- Rotunno, R., J. B. Klemp, and M. L. Weisman, 1988: A theory for strong, long-lived squall lines. *J. Atmos. Sci.*, **45**, 463–485, doi:[10.1175/1520-0469\(1988\)045<0463:ATFSLL>2.0.CO;2](https://doi.org/10.1175/1520-0469(1988)045<0463:ATFSLL>2.0.CO;2).
- Skamarock, W. C., and Coauthors, 2008: A description of the Advanced Research WRF version 3. NCAR Tech. Note NCAR/TN-475+STR, 113 pp., doi:[10.5065/D68S4MVH](https://doi.org/10.5065/D68S4MVH).
- Song, I.-S., H.-Y. Chun, and T. P. Lane, 2003: Generation mechanisms of convectively forced internal gravity waves and their propagation to the stratosphere. *J. Atmos. Sci.*, **60**, 1960–1980, doi:[10.1175/1520-0469\(2003\)060<1960:GMOCFI>2.0.CO;2](https://doi.org/10.1175/1520-0469(2003)060<1960:GMOCFI>2.0.CO;2).
- Stephan, C. C., M. J. Alexander, M. Hedlin, C. D. de Groot-Hedlin, and L. Hoffmann, 2016: A case study on the far-field properties of propagating tropospheric gravity waves. *Mon. Wea. Rev.*, **144**, 2947–2961, doi:[10.1175/MWR-D-16-0054.1](https://doi.org/10.1175/MWR-D-16-0054.1).
- Trier, S. B., G. S. Romine, D. A. Ahijevych, R. J. Trapp, R. S. Schumacher, M. C. Coniglio, and D. J. Stensrud, 2015: Mesoscale thermodynamic influences on convection initiation near a surface dryline in a convection-permitting ensemble. *Mon. Wea. Rev.*, **143**, 3726–3753, doi:[10.1175/MWR-D-15-0133.1](https://doi.org/10.1175/MWR-D-15-0133.1).
- Wang, Q.-W., and M. Xue, 2012: Convective initiation on 19 June 2002 during IHOP: High-resolution simulations and analysis of the mesoscale structures and convection initiation. *J. Geophys. Res.*, **117**, D12107, doi:[10.1029/2012JD017552](https://doi.org/10.1029/2012JD017552).
- Weckwerth, T. M., and D. B. Parsons, 2006: A review of convection initiation and motivation for IHOP_2002. *Mon. Wea. Rev.*, **134**, 5–22, doi:[10.1175/MWR3067.1](https://doi.org/10.1175/MWR3067.1).
- , and Coauthors, 2004: An overview of the International H₂O Project (IHOP_2002) and some preliminary highlights. *Bull. Amer. Meteor. Soc.*, **85**, 253–277, doi:[10.1175/BAMS-85-2-253](https://doi.org/10.1175/BAMS-85-2-253).
- Weisman, M. L., and R. Rotunno, 2004: “A theory for strong long-lived squall lines” Revisited. *J. Atmos. Sci.*, **61**, 361–382, doi:[10.1175/1520-0469\(2004\)061<0361:ATFSL>2.0.CO;2](https://doi.org/10.1175/1520-0469(2004)061<0361:ATFSL>2.0.CO;2).
- , W. C. Skamarock, and J. B. Klemp, 1997: The resolution dependence of explicitly modeled convective systems. *Mon. Wea. Rev.*, **125**, 527–548, doi:[10.1175/1520-0493\(1997\)125<0527:TRDOEM>2.0.CO;2](https://doi.org/10.1175/1520-0493(1997)125<0527:TRDOEM>2.0.CO;2).
- Weiss, C. C., and H. B. Bluestein, 2002: Airborne pseudo-dual Doppler analysis of a dryline-outflow boundary intersection. *Mon. Wea. Rev.*, **130**, 1207–1226, doi:[10.1175/1520-0493\(2002\)130<1207:APDDAO>2.0.CO;2](https://doi.org/10.1175/1520-0493(2002)130<1207:APDDAO>2.0.CO;2).
- Wilson, J. W., and W. E. Schreiber, 1986: Initiation of convective storms at radar-observed boundary-layer convergence lines. *Mon. Wea. Rev.*, **114**, 2516–2536, doi:[10.1175/1520-0493\(1986\)114<2516:IOCSAR>2.0.CO;2](https://doi.org/10.1175/1520-0493(1986)114<2516:IOCSAR>2.0.CO;2).
- , and C. K. Mueller, 1993: Nowcasts of thunderstorm initiation and evolution. *Wea. Forecasting*, **8**, 113–131, doi:[10.1175/1520-0434\(1993\)008<0113:NOTIAE>2.0.CO;2](https://doi.org/10.1175/1520-0434(1993)008<0113:NOTIAE>2.0.CO;2).

- , and R. D. Roberts, 2006: Summary of convective storm initiation and evolution during IHOP: Observational and modeling perspective. *Mon. Wea. Rev.*, **134**, 23–47, doi:[10.1175/MWR3069.1](https://doi.org/10.1175/MWR3069.1).
- , G. Foote, N. Crook, J. Fankhauser, C. Wade, J. Tuttle, C. Mueller, and S. Krueger, 1992: The role of boundary-layer convergence zones and horizontal rolls in the initiation of thunderstorms: A case study. *Mon. Wea. Rev.*, **120**, 1785–1815, doi:[10.1175/1520-0493\(1992\)120<1785:TROBL>2.0.CO;2](https://doi.org/10.1175/1520-0493(1992)120<1785:TROBL>2.0.CO;2).
- , N. A. Crook, C. K. Mueller, J. Sun, and M. Dixon, 1998: Nowcasting thunderstorms: A status report. *Bull. Amer. Meteor. Soc.*, **79**, 2079–2099, doi:[10.1175/1520-0477\(1998\)079<2079:NTASR>2.0.CO;2](https://doi.org/10.1175/1520-0477(1998)079<2079:NTASR>2.0.CO;2).
- Xue, M., and W. J. Martin, 2006: A high-resolution modeling study of the 24 May 2002 dryline case during IHOP. Part II: Horizontal convective rolls and convective initiation. *Mon. Wea. Rev.*, **134**, 172–191, doi:[10.1175/MWR3072.1](https://doi.org/10.1175/MWR3072.1).
- Ziegler, C. L., and E. N. Rasmussen, 1998: The initiation of moist convection at the dryline: Forecasting issues from a case study perspective. *Wea. Forecasting*, **13**, 1106–1131, doi:[10.1175/1520-0434\(1998\)013<1106:TIOMCA>2.0.CO;2](https://doi.org/10.1175/1520-0434(1998)013<1106:TIOMCA>2.0.CO;2).